Suppression of PIK3CA-driven epileptiform activity by acute pathway control

Achira Roy[1,*], Victor Z. Han[1,2], Angela M. Bard[1], Devin T. Wehle[1,3], Stephen E. P. Smith[1,4], Jan-Marino Ramirez[1,4,5,6], Franck Kalume[1,5,7], Kathleen J. Millen[1,4,*]

[1]Center for Integrative Brain Research, Seattle Children's Research Institute, Seattle, Washington, USA; [3]Graduate Program in Neuroscience and Departments of [2]Biology, [4]Pediatrics, [5]Neurological Surgery, [6]Physiology and Biophysics, and [7]Pharmacology, University of Washington, Seattle, Washington, USA.

*Correspondence: Kathleen J. Millen, PhD
Seattle Children's Research Institute,
Center for Integrative Brain Research
1900 9th Avenue, Mailstop: JMB-10,
Seattle, WA, USA. ZIP: 98101
Email: kathleen.millen@seattlechildrens.org; Tel: +1-206-884-3225

Achira Roy, PhD
Seattle Children's Research Institute
Center for Integrative Brain Research
1900 9th Avenue, Mailstop: JMB-10,
Seattle, WA, USA. ZIP: 98101

Email: achira.roy@gmail.com; Tel: +1-206-884-5490

Competing Interests Statement: All authors read and approved the final manuscript. None of the authors have competing interests.

Short title: Acute suppression of PIK3CA-driven epilepsy

Keywords: PI3K; epilepsy; mouse model; preclinical drug screens; BKM120; RAD001; AZD5363; intractable; pyramidal neuron; hippocampus; electrophysiology

Number of Figures: 5

Number of Tables: 1

Number of Figure supplements: 7

ABSTRACT

Patients harboring mutations in the PI3K-AKT-MTOR signaling pathway often develop a spectrum of neurodevelopmental disorders including epilepsy. A significant proportion of them remain unresponsive to conventional anti-seizure medications. Understanding mutation-specific pathophysiology is thus critical for molecularly targeted therapies. We previously determined that mouse models expressing patient-related activating mutation in *PIK3CA* are epileptic and acutely treatable with PI3K inhibition, irrespective of dysmorphology (Roy et al. 2015). Using the same mutant model, we have now identified physiological mechanisms underlying the dysregulated neuronal excitability and its acute attenuation. We show that Pik3ca-driven hyperexcitability in hippocampal pyramidal neurons is mediated by changes in multiple non-synaptic, cell-intrinsic properties. These are distinct from mechanisms driving epilepsy in TSC/RHEB models. Further, we report that acute inhibition of PI3K or AKT, but not MTOR, suppresses the intrinsic epileptiform nature of the mutant neurons. These data represent an important step towards precision therapeutics against intractable epilepsy, using pathway drugs originally developed as anti-cancer agents.

53 **INTRODUCTION**

54 Mutations in the PI3K-AKT-MTOR signaling pathway, long studied for roles in
55 cancer (Madsen 2020; Yang et al. 2019), also cause clinically important developmental
56 brain overgrowth syndromes. Affected individuals display phenotypes ranging from
57 dysplastic megalencephaly, hemimegalencephaly and focal cortical dysplasia, as well
58 as comorbidities including hydrocephalus, autism and intellectual disability (Bast et al.
59 2006; Blumcke et al. 2011; Mirzaa 2018; Stafstrom and Carmant 2015; Dobyns and
60 Mirzaa 2019; Crino 2016). These mutations also cause focal epilepsy, representing 25-
61 50% of all cases of intractable (treatment-resistant) epilepsy in children (Bast et al.
62 2006; Blumcke et al. 2011; Kim and Lee 2019; Mirzaa 2018; Stafstrom and Carmant
63 2015). Traditionally, anti-seizure drugs targeting generic ion channels are identified by
64 evoking acute seizures in wild-type rodents (Wilcox, West, and Metcalf 2020; Kehne et
65 al. 2017; Barker-Haliski and White 2019), which do not mimic clinical epilepsies
66 associated with specific genetic mutations and hence are largely ineffective. Since PI3K
67 pathway mutations are now known to cause intractable epilepsy, repurposing pathway-
68 targeted anti-cancer drugs offers a tantalizing opportunity to fundamentally shift the
69 therapeutic approach towards intractable epilepsy. Presently, the MTOR inhibitor
70 rapamycin and its analogs are the sole pathway-related drugs used clinically to treat
71 epilepsy, primarily in patients with rare *TSC1/2* deletion mutations which enhance
72 downstream MTOR signaling(Stafstrom 2019; Crino 2016; Kim and Lee 2019). Yet,
73 these treatments remain effective only to a modest degree, suggesting that MTOR
74 activation may not be the sole arm of this complex signaling pathway accounting for all
75 PI3K pathway-driven epilepsies (Cho 2011; Meng et al. 2013; Roy et al. 2015).

76 Here we assess acute mechanisms driving epileptiform activity in *Nestin-*
77 *cre;Pik3ca*^{E545K} mouse model harboring a patient-related activating mutation in *Pik3ca*,
78 encoding the p110a catalytic subunit of PI3K (Roy et al. 2015). We report that Pik3ca
79 overactivation causes intrinsic neuronal changes leading to hyperexcitability. We further
80 establish that this epileptiform activity is acutely dependent on AKT, but not MTOR,
81 regulation. Our study defines key aspects of acute neuronal dysregulation in an
82 important genetic epilepsy model, which we leverage to repurpose the available PI3K
83 pathway inhibitors against intractable epilepsy.

RESULTS

In vivo recordings demonstrate network hyperexcitability in mutant CA1

Pik3ca mutant mouse models recapitulate patient phenotypes including brain overgrowth, cortical dysplasia, hydrocephalus and epilepsy, with phenotypic severity dependent on the mutant allele and its time of activation (Roy et al. 2019; Roy et al. 2015). Moreover, this developmental epilepsy is dissociable from dysmorphology and acutely suppressible by 1-hour *in vivo* administration of the pan-PI3K inhibitor BKM120 (Maira et al. 2012; Roy et al. 2015). To identify the underlying dynamic mechanisms, we performed *in vivo* and *in vitro* electrophysiological studies primarily focused on hippocampal pyramidal neurons, since the connection between epilepsy and hippocampal pathophysiology is well documented in patients and model systems, including ours (Roy, Millen, and Kapur 2020; Chatzikonstantinou 2014; Mazumder, Patial, and Singh 2019; Berdichevsky et al. 2013; Roy et al. 2015).

We investigated *in vivo* changes in the hippocampal CA1 network activity of ~P70 *Nestin-cre;Pik3ca*^{E545K} mutant mice relative to control littermates using local field potential (LFP) recordings, while simultaneously monitoring cortical surface activity by electrocorticography (ECoG). These recordings showed spontaneous interictal spike activity either restricted to the cortex or the hippocampus exclusively, or concurrent to the two regions in the mutant mice (Figure 1A-C; Figure 1 – figure supplement 1A-D). A broad spectrum of spike patterns was observed, consisting of single or groups of interictal spikes, the simplest identifiable unit of epileptiform activity (McCormick and Contreras 2001), as well as trains of sharp spikes, low-frequency slow waves or high-frequency low-amplitude “brushing events”. These epileptiform events were observed

107 exclusively in the mutant mice. Within the mutant group, the event frequency was
108 significantly higher in the hippocampus than in the neocortex (Figure 1D). Power
109 spectrum analyses revealed that the mutant hippocampi exhibit significantly higher
110 power in the gamma frequency bands (Figure 1E-H), which is often indicative of seizure
111 onset (Hughes 2008; Lee, Spencer, and Spencer 2000). These observations indicate
112 that Pik3ca overactivation caused significant neural hyperexcitability in our mice,
113 predominantly in the hippocampus.
114

115 **Mutant CA1 has elevated, acutely regulatable network excitability *in vitro***

116 To assess the physiological aspects of Pik3ca-driven epilepsy at the tissue level,
117 we performed hippocampal extracellular field recordings in acute forebrain slices. First,
118 we conducted these recordings in P16-20 CA1 pyramidal layer, across a potassium
119 concentration gradient in the recording buffer ([K^+]: 3 mM to 12 mM; Figure 2A-C). This
120 standard model shifts wild-type neuronal network from a silent state to tonic spiking and
121 then to bursting, followed by a depolarization block at very high levels of [K^+], thus
122 mimicking a seizure-like response (Filatov et al. 2011). Compared to controls, mutant
123 slices exhibited a narrow range of hypersynchronous bursting and an elevated mean
124 baseline measured from the integrated trace, especially from 8mM to 12mM [K^+] (Figure
125 2B,C; Figure 2 – figure supplement 2A). Mutant slices also showed significantly
126 enhanced relative peak amplitudes (at 8-9 mM [K^+]; Figure 2 – figure supplement 2B).
127 Thus, the mutation lowers the excitability threshold and a depolarization block is
128 reached faster than in controls. Further, acute extracellular application of BKM120
129 suppressed the hypersynchronous ictal bursts in the mutant CA1 field in 20-30 min, with

130 minimal physiological effect on control brains (Figure 2D,E). These data provide
131 evidence of a Pik3ca-driven active mechanism.
132
133 **Mutant CA1 and CA3 pyramidal neurons are hyperexcitable**
134 Next, we investigated mechanisms driving the mutant epileptiform activity at the
135 cellular level, using whole-cell patch-clamp recordings from CA1 and CA3 pyramidal
136 neurons in P16-20 control and mutant brains (Figure 3A). Silent and spontaneously
137 firing, tonic and burst-generating neurons were detected in both control and mutant
138 slices (Figure 3B,C). However, mutant slices had a significantly higher proportion of
139 burst-generating cells in both regions and lower proportion of tonic-firing cells in mutant
140 CA1 compared to controls (Figure 3D,E). Additionally, we observed significantly higher
141 tonic spike frequencies in mutant CA1 and CA3 and higher burst frequency in mutant
142 CA1, compared to controls (Figure 3F,G). Burst-generating cells demonstrated multiple
143 burst types. Specifically, we identified burst clusters and two types of plateau-bursts:
144 paroxysmal depolarization shift (PDS) and non-PDS waveforms (Figure 3 – figure
145 supplement 1A). We defined burst cluster as a multi-spike burst activity of random
146 nature without a plateau potential; these were only observed in mutant slices (Figure 3 –
147 figure supplement 1B). Plateau-bursts with depolarization shift resulting in sodium-spike
148 inactivation were termed as PDS “bursting cells”. These depolarization shifts have
149 previously been implicated as the intracellular correlate of *in vivo* interictal spikes
150 (Marcuccilli et al. 2010; McCormick and Contreras 2001; Kubista, Boehm, and Hotka
151 2019; Tryba et al. 2019). We defined non-PDS bursts as those where plateau potential
152 developed in absence of prominent sodium-spike inactivation. No significant differences

153 between control and mutant hippocampal pyramidal cells were observed with respect to
154 average burst duration or inter-burst interval (Figure 3 – figure supplement 1C-E).
155 However, the plateau potential shift (PPS), defined here as the difference of the steady
156 state plateau potential and the resting membrane potential (RMP), was significantly
157 larger in mutant CA1 but not in CA3, relative to respective controls (Figure 3H,H'). This
158 was despite similar RMP across control and mutant hippocampal neurons (Figure 3 –
159 figure supplement 2A-C). The evoked current-clamp recordings further validated the
160 spontaneous activity results, especially by displaying significantly higher percentage of
161 burst-generating pyramidal neurons in the mutant hippocampus (Figure 3I-M).
162 Incidentally, no significant difference in membrane intrinsic properties like input
163 resistance, rheobase current and burst-threshold current, as well as evoked tonic spike
164 frequencies (for the tested 0-90pA range), was observed between control and mutant
165 cells (Table 1; Figure 3 – figure supplement 2D-F). But the decay time constant for
166 mutant CA3 neurons was significantly longer than that in mutant CA1 and control
167 groups (Table 1). With similar resistance, this implied that mutant CA3 neurons have
168 higher membrane capacitance than other cell groups. Together, these data demonstrate
169 that Pik3ca overactivation results in intracellular hyperexcitability, with some distinct cell
170 type-specific effects.

171 To determine whether the Pik3ca-related hyperexcitability is driven by altered
172 synaptic interactions or other intrinsic properties, we assessed the effects of channel
173 and receptor blockers on mutant hippocampal physiology. Blocking glutamatergic inputs
174 by extracellular administration of NMDA and non-NMDA receptor-antagonists, 3-((±)2-
175 carboxypiperazin-4yl) propyl-1-phosphate (CPP) and 6-cyano-7-nitroquinoxaline-2,3-

176 dione (CNQX) respectively, had no overt physiological effect on the majority of mutant
177 hippocampal neurons (Figure 4 – figure supplement 1A-C,E,F,H-K). Similarly, blocking
178 inhibitory synaptic inputs with gabazine did not significantly alter the mutant firing
179 patterns, spike frequencies or PPS (Figure 4 – figure supplement 1A,D,G,L). The
180 proportion of mutant CA1 neurons affected by these channel blockers was
181 comparatively less than that in CA3. Our data lead to the important conclusion that
182 Pik3ca-driven epileptiform activity is primarily not dependent on synaptic transmission.
183 In contrast, inhibition of calcium (Ca^{2+})-dependent inward current by extracellular
184 cadmium (Cd^{2+}) attenuated the paroxysmal bursts and reduced burst frequency and
185 PPS (Figure 4A-D), indicating a calcium channel-dependent mechanism underlying the
186 Pik3ca-dependent epileptiform activity. Intracellular cesium blocked potassium channels
187 and related currents, altering the intrinsic firing pattern in both control and mutant
188 hippocampal slices. Specifically, compared to regular baseline recordings, intracellular
189 cesium considerably reduced the proportion of tonic-firing cells in both CA1 and CA3
190 (Figure 4E-H, compare to Figure 3D,E). Unlike the spontaneous recordings, intracellular
191 cesium prompted the burst frequency in mutant CA1 to normalize and in mutant CA3 to
192 significantly rise, relative to respective controls (Figure 4I, compare to Figure 3G).
193 Intracellular cesium also normalized the mutant PPS to control levels (Figure 4J,
194 compare to Figure 3H). No overt effect on RMP or input resistance was seen in cesium-
195 treated control and mutant cells (Figure 4K,L). We conclude that Pik3ca-related
196 epileptiform activity is primarily caused by a complex set of altered non-synaptic cell-
197 intrinsic properties.
198

199 **Acute treatment of epileptiform activity with PI3K pathway drugs**

200 The acute suppression of epileptiform activity in *Nestin-cre;Pik3ca*^{E545K} mice by
201 BKM120, both *in vivo* (Roy et al. 2015) and at the tissue level, prompted us to dissect
202 the downstream pathway dynamics using inhibitors at the cellular level, in order to
203 coarsely determine their mechanistic roles and identify new therapeutic targets to treat
204 intractable epilepsy (Figure 5A). Acute extracellular administration of BKM120 or the
205 pan-AKT inhibitor AZD5363 (Davies et al. 2012) resulted in a large-scale and significant
206 alteration of firing pattern, frequencies and a relative reduction of PPS, sometimes
207 leading to gradual silencing of the recorded neurons (Figure 5B-I,I'). Neither drug had
208 any significant effect on neuronal RMP or tonic rheobase current (Figure 5 – figure
209 supplement 1A,B,E,F). In contrast to BKM120, acute AKT downregulation by AZD5363
210 significantly reduced the mutant burst duration and inter-burst interval (Figure 5 – figure
211 supplement 1C,D,G,H). Further, AZD5363 altered the physiology of all mutant CA3
212 neurons much faster (~8 min) than BKM120 (~32 min); however, both drugs changed
213 the intracellular activity of ~50% cells within 4 min (Figure 5 – figure supplement 1I,J).
214 AZD5363 also blocked spontaneous bursts in mutant neurons faster than BKM120
215 (Figure 5 – figure supplement 1K). Thus, acute regulation of both PI3K and AKT activity
216 directly suppressed *Pik3ca*^{E545K}-driven epileptiform neuronal activity. In contrast, acute
217 administration of the MTOR inhibitor RAD001 (everolimus) (Cho 2011; Krueger et al.
218 2010) showed no overt effect on the mutant RMP, tonic or burst firing patterns,
219 frequencies, average PPS, burst duration, inter-burst interval and rheobase current
220 (Figure 5J-M, Figure 5 – figure supplement 2A-D). This was despite western blot
221 confirmation that acute treatment of forebrain slices with RAD001 modulated direct

222 downstream targets of MTOR (Figure 5 – figure supplement 2E-G). In summary, our
223 study demonstrates that epileptiform activity caused by Pik3ca overactivation is based
224 on multiple intrinsic electrophysiological characteristics that are acutely modifiable by
225 downregulating PI3K and AKT activity, but not MTOR.

226 **DISCUSSION**

227 Activating mutations in the PI3K-AKT-MTOR pathway commonly cause pediatric
228 intractable epilepsy (Kim and Lee 2019; Dobyns and Mirzaa 2019); yet the underlying
229 mechanisms remain largely undefined. Using our *Nestin-cre;Pik3ca*^{E545K} model, we now
230 establish that Pik3ca-dependent neuronal hyperexcitability in hippocampal pyramidal
231 neurons is driven primarily by intrinsic neuronal mechanisms. Acute attenuation of
232 epileptiform activity by inhibiting AKT but not MTOR also reveals a previously unknown
233 role of PI3K signaling in neuronal homeostasis. Our mouse model of human intractable
234 epilepsy is now validated across whole animal, tissue, and cellular levels.

235 Epileptiform activity is typically marked by increased tonic depolarizations and/or
236 quasiperiodic bursts, mediated by intrinsic membrane properties, ephaptic or
237 synaptic/circuit-level interactions (McCormick and Contreras 2001; Dudek, Yasumura,
238 and Rash 1998). We confirmed enhanced interictal spike frequency and diverse,
239 synchronized epileptiform spike patterns in the mutant brains *in vivo*, predominantly in
240 the hippocampus. This is consistent with studies of *PIK3CA* variants in brain tumors and
241 mouse models with patient-related *Pik3r2* mutations, which are less common causes of
242 intractable epilepsy (Yu et al. 2020; Shi et al. 2020). Our *in vitro* analyses revealed
243 intracellular correlates of epileptiform activity and enhanced firing frequencies in the
244 mutant hippocampal pyramidal neurons. Relative to controls, *Pik3ca*^{E545K} neurons
245 exhibited significantly higher proportions of bursting cells and higher heterogeneity in
246 burst patterns, including burst clusters and PDSs. A prior study showed that human
247 neurons from surgically resected neocortical samples of pediatric patients with focal
248 cortical dysplasia (FCD) exhibited remarkably similar burst characteristics (Marcuccilli et

249 al. 2010). These samples were not genotyped; however, since most cases of FCD and
250 epilepsy result from variants in PI3K pathway genes (Mirzaa 2018), such cross-species
251 phenotypic correlation is remarkable and emphasizes the clinical relevance of our
252 mouse model.

253 The PI3K-AKT-MTOR pathway is also known to influence synaptogenesis and
254 neuronal plasticity (Sanchez-Alegria et al. 2018). For example, neocortical samples
255 from patient and mouse models with *TSC* mutations exhibit synaptic input-mediated
256 epileptogenic hyperexcitability (Wang et al. 2007). However, blocking glutamatergic
257 (NMDA and non-NMDA) or GABAergic synaptic inputs showed no significant effect on
258 the neuronal activity in our mutant brain slices. We acknowledge that altered neuronal
259 circuitry may be relevant to Pik3ca-mediated epilepsy, but our data demonstrate that
260 altered synaptic interactions are at least not primary mediators of dynamic hippocampal
261 neuronal hyperexcitability.

262 Significant reduction of burst-generating cells, burst frequency and PPS by
263 blocking voltage-dependent calcium or potassium channels indicate that *Pik3ca*^{E545K}-
264 driven epileptiform activity is predominantly mediated by multiple altered cell-intrinsic
265 properties. Yet, some cell-intrinsic properties, such as burst frequencies, PPS and time
266 constants, are distinctly different between mutant CA1 and CA3 neurons. Since all
267 neurons do not react uniformly to either pathway overactivation or Cd^{2+}/Cs^{+}-dependent
268 channel inhibition, current anti-seizure drugs that typically target single ion channels
269 cannot address the heterogeneous dysregulation, thus potentially explaining epileptic
270 intractability in this patient population. It is intriguing to note that intercellular signaling
271 heterogeneity involving PI3K-AKT-MTOR pathway was also reported by a recent

272 quantitative study that highlighted its potential relevance to human disorders, such as
273 insulin resistance (Norris et al. 2021).
274 PI3K-AKT-MTOR inhibitors developed to treat cancer potentially represent novel
275 anti-seizure therapeutics (Cardamone et al. 2014; Lindhurst et al. 2015; Maira et al.
276 2012; Zou et al. 2020; Forde et al. 2021; Venot et al. 2018). Rapamycin and its analogs,
277 that are currently in clinical use to treat epilepsy in TSC patients, curbed epileptiform
278 activity in mouse models harboring *TSC1/2*, *RHEB, MTOR* or *PTEN* mutations when
279 administered long-term (>7-day) (Curatolo and Moavero 2013; Crino 2016; Lasarge and
280 Danzer 2014; Stafstrom 2019; Kim and Lee 2019). In contrast, we show acute inhibition
281 of epileptiform activity by BKM120 *in vitro*, confirming our previous *in vivo* finding (Roy
282 et al. 2015). We also demonstrate that acute AKT inhibition with AZD5363 has similar
283 effects. This first preclinical study using AZD5363 to treat epilepsy shows that acute
284 Pik3ca-driven epileptiform mechanism is predominantly AKT-dependent, limiting roles
285 for other PI3K targets. Intriguingly, rapamycin analog RAD001 had minimal acute effect
286 in our model. While elevated MTOR activity is known to be epileptogenic (Crino 2016;
287 Kim and Lee 2019), our data suggest that alternate PI3K-AKT targets acutely regulate
288 neuronal hyperexcitability. This study establishes an important foundation to determine
289 active pathway-driven cellular mechanisms and to assess the plethora of available PI3K
290 pathway inhibitors, facilitating new molecularly rational therapeutic interventions for
291 intractable epilepsy.

292 **MATERIALS AND METHODS**

293 **Mice**

294 The following mouse lines were used: *Nestin-cre* (Jackson Labs, Bar Harbor, Maine,
295 USA; Stock #003771, RRID: IMSR_JAX:003771), conditional *Pik3ca*^{E545K} knock-in
296 (Robinson et al. 2012). *Nestin-cre* and *Pik3ca*^{E545K} mouse lines were maintained in
297 C57BL/6 and FVB backgrounds respectively. We have designated *Nestin-*
298 *cre;Pik3ca*^{E545K} conditional mutant mice as "*Pik3ca* mutants" or "mutants" throughout the
299 manuscript.

300 All mice were housed in Optimice cages with aspen bedding at the Seattle
301 Children's Research Institute's specific pathogen-free (SPF) vivarium facility (light "ON":
302 6am – 8pm). Noon of the day of vaginal plug was designated as embryonic day 0.5
303 (E0.5). The day of birth was designated as postnatal day 0 (P0). Genotyping by PCR
304 was done using separate sets of primers for the *Cre* coding region and the *Pik3ca*^{E545K}
305 allele, as previously described(Roy et al. 2015). All mouse procedures were approved
306 and conducted in accordance with the guidelines laid down by the Institutional Animal
307 Care and Use Committees (IACUC) of Seattle Children's Research Institute, Seattle,
308 WA, USA. ARRIVE guidelines have been followed for reporting work involving animal
309 research.

310

311 ***In vivo* electrophysiology**

312 5 control and 6 *Nestin-cre;Pik3ca*^{E545K} mutant mice (age: ~P70) were used for *in vivo*
313 regular and depth-electrode electrophysiology experiments. We saw no sex-dependent
314 data correlation (Roy et al. 2015).

315 *Electrode implantation surgery:* Mice underwent survival surgery to implant ECoG,
316 EMG, and hippocampal depth electrodes under isoflurane anesthesia using similar
317 procedures as reported in our prior work (Bolea et al. 2019; Roy et al. 2015). The ECoG
318 electrodes consisted of silver wire (diameter: 130 μm bare; 180 μm coated) attached to
319 micro screws. The ECoG electrodes were implanted bilaterally through small cranial
320 burr holes above the somatosensory cortices. A similar reference electrode was placed
321 above the cerebellum following the same procedure. The depth electrodes were made
322 of 2 fine twisted tungsten wires (30um nylon coated, California fine wire) and implanted
323 in the hippocampal CA1 region (coordinates: -2.0 mm anteroposterior, 1.5 mm
324 mediolateral, 1.9 mm dorsoventral in reference to bregma) to record local field potential
325 (LFP). All electrodes were connected to interface connector and fixed to the skull with
326 dental cement (Lang Dental Manufacturing Co., Inc., Wheeling, IL). Mice were allowed
327 to recover from surgery for 2-3 days.

328 *Video, electroencephalagraphy and local field potential (Video-EEG-LFP) recording:*
329 Simultaneous video-EEG-LFP recordings were collected from conscious mice on
330 PowerLab 8/35 and 16/30 data acquisition units, using LabChart 7.3.3 software (AD
331 Instruments, Colorado Spring, USA). ~6 hours of baseline ECoG tracings were visually
332 reviewed for the presence of spontaneous epileptiform events, as previously studied
333 (Kalume 2013; Liautard et al. 2013; Roy et al. 2015). All bioelectrical signals were
334 acquired at a 20 KHz sampling rate. The ECoG signals were processed with a 1-70 Hz
335 bandpass filter and the LFP signal with a 5 Hz high-pass filter. Interictal spikes were
336 identified as transient, clearly distinguished from background activity, with pointed peak
337 and slow wave. Myoclonic seizures were identified as shock-like muscular jerks on

338 video, associated with a spike or polyspike-wave complex on EEG. Power spectral
339 analysis and visual inspection of the data were conducted to characterize the EEG
340 activity in different frequency bands and identify epileptiform event on the ECoG and
341 local CA1 field recordings using the Labchart 8.2 software.
342
343 ***In vitro* electrophysiology**
344 *Slice preparation:* Postnatal (P16-20) pups were anesthetized briefly in a closed
345 chamber by administering isoflurane (5% flow rate) or CO_2 (constant flow rate: 10-30%
346 of chamber vol/min); then perfused transcardially with ice-cold low Na^+-buffer ("slicing
347 solution," which included the following: 252 mM sucrose, 2 mM KCl, 2 mM $MgCl_2$, 2.6
348 mM $CaCl_2$, 1.2 mM NaH_2PO_4, 26 mM $NaHCO_3$, and 15 mM glucose, with the pH
349 adjusted to 7.4 and the osmolarity to 310 ± 5 mOsm). Brain was dissected out by
350 separating the head and cutting along the skull sutures using fine scissors and forceps.
351 The forebrain was isolated in ice-cold, oxygenated (95% O_2, 5% CO_2) slicing solution. A
352 slanted (~15° from vertical) agar block was secured on a specimen tray as a support for
353 the brain during slicing. The isolated forebrain was glued with cyanoacrylate in the
354 orientation depending on the type of slices we wanted; and then placed in the vibratome
355 for slicing. Slicing was proceeded until hippocampal landmark was visible. For coronal
356 slices (extracellular recordings), the forebrain was placed such that its antero-posterior
357 (A-P) axis was perpendicular to the specimen tray/vibratome blade, and olfactory bulb
358 distal to the tray surface. For horizontal slices (whole-cell recordings), the forebrain was
359 oriented such that it's A-P axis was parallel to the specimen tray and ventral side
360 (hippocampal side) was on the top, distal to the tray surface. Once the hippocampus

361 became visible, thick, acute slices (thickness: 350μm for extracellular recordings, 200-
362 250μm for whole-cell patch clamp recordings) were taken and incubated in ice-cold
363 slicing solution continuously oxygenated with 95% O_2/5% CO_2. After cutting, slices were
364 immediately returned to the same solution and maintained in a warm bath (28 ± 0.5°C)
365 for recovery. After 30 min, they were transferred into regular artificial cerebrospinal fluid
366 (aCSF), composed of the same components as slicing solution except for the
367 replacement of sucrose with 126 mM NaCl. Slices were then kept at room temperature,
368 continuously superfused with oxygenated aCSF, until recording. Given that *Pik3ca*^{E545K}
369 mutant is megalencephalic, a greater number of hippocampal/forebrain sections were
370 obtained. However, care was taken so that the dorso-ventral plane(s) used for recording
371 was always comparable between control and mutant slices. No randomization was
372 used. Tissue collection was not performed blind since the mice were subjected to
373 genotyping and drug administration.

374 *Recording:* Slices were transferred into a recording chamber, continuously superfused
375 with oxygenated aCSF, for extracellular or intracellular whole-cell recordings. The
376 pClamp software suite (Molecular Devices; RRID:SCR_011323) was used for data
377 acquisition and analysis. Signals were amplified (MultiClamp 700A, Axon Instruments,
378 Molecular Devices, USA), digitized (D1322A, Axon Instruments, Molecular Devices,
379 USA), and stored in a computer for post-hoc analysis.

380 *a) Extracellular recording:* To determine if hippocampal neuronal populations in
381 *Pik3ca*^{E545K} mutants have different electrochemical signatures than controls,
382 extracellular population recordings were performed on CA1 hippocampal pyramidal
383 neuronal layer in acute 350 μm-thick coronal brain slices of ~P16-20 *Pik3ca*^{E545K} mutant

384 and control littermates (n=6). To induce epileptiform activity in the slices, we increased
385 potassium concentration ([K^+]) (Borck and Jefferys 1999; Leschinger et al. 1993) from 3
386 mM to 12 mM, in 1mM increments at 30°C. This standard model induces wild-type
387 neurons to transition from a silent neuronal state to tonic spiking and then to bursting,
388 followed by depolarization block at very high [K^+] (Filatov et al. 2011).
389 *b) Intracellular recording:* Horizontal hemi-forebrain slices with prominent
390 hippocampus were used for intracellular whole-cell visual patch-clamp experiments.
391 Slices transferred to the recording chamber were maintained at 30-34°C, constantly
392 superfused with oxygenated aCSF. Borosilicate glass capillaries/pipettes for patch-
393 clamp recording had electrode resistance (R_e) optimally kept around 5-8 MΩ, after being
394 filled with internal solution containing the following: potassium gluconate (~132 mM),
395 KCl (5 mM), HEPES (10 mM), EGTA (5 mM), $CaCl_2.H_2O$ (0.5 mM), $MgCl_2$ (2 mM),
396 disodium phosphocreatine (5 mM), disodium-ATP (4 mM), trisodium-GTP (0.5 mM),
397 EGTA (5 mM). Cells were visualized under brightfield optics using the 40X water-
398 immersion objective of an upright microscope (Olympus, BX51WI). The patch electrode
399 was advanced toward the target cells by a micromanipulator (MP-225, Sutter Instrument
400 Company, USA) and 1 GΩ seal was established, typically by a small negative pressure,
401 with the membrane ruptured by gentle suction and/or zap pulses. Whole-cell patch-
402 clamp recording was performed from cell bodies of pyramidal neurons of hippocampal
403 CA1 and CA3 respectively. Following intracellular recording protocols were also used:
404 i. Spontaneous gap-free recordings in current (I)-clamp: cells were typically tested
405 at resting conditions (without current injection) unless noticed otherwise.

406 ii. Evoked I-clamp steps protocol: current steps start at -50 pA, incremental 10 pA,
407 duration; 300 ms; 15 steps (-90 to +50 pA) were recorded across experiments.
408

409 **Acute chemical assays**

410 *Channel blockers:* Chemicals inhibiting specific ion channels were introduced in the
411 bath/recording chamber during *in vitro* whole-cell recordings to compare different
412 components contributing to the neural activity in control and *Pik3ca*^{E545K} mutant mice. To
413 block all fast-synaptic excitatory transmission, 3-((±)2-carboxypiperazin-4yl) propyl-1-
414 phosphate (CPP, NMDA receptor antagonist, 20 μM; Tocris Bioscience, UK) and 6-
415 cyano-7-nitroquinoxaline-2,3-dione (CNQX, AMPA/kainite (non-NMDA) receptor
416 antagonist, 20 μM, diluted in DMSO; Alomone Labs, Israel) were introduced in the bath
417 (Lehmann et al. 1987; Lester et al. 1989). SR95531 hydrobromide (Gabazine, $GABA_A$
418 receptor antagonist, 10 μM, Tocris Bioscience, UK) were used to block inhibitory
419 synaptic transmission. Divalent cation Cd^{2+} ($CdCl_2$, 100 μM; Sigma-Aldrich, USA)
420 (Boissard et al. 2002) was used to depress synaptic transmission and block inward
421 calcium-selective current, isolating the outward K^+ current. To block voltage-dependent
422 K^+ channels, intracellular administration of cesium (Covey, Kauer, and Casseday 1996)
423 was done by replacing potassium gluconate with cesium gluconate in the internal
424 solution while maintaining the same osmolarity.

425 *PI3K pathway drugs:* Drugs regulating PI3K pathway were added to the circulating
426 recording buffer, thus getting acutely administered in the brain slice placed in the
427 recording chamber. For protein analyses, these were added at identical concentration to
428 the brain slices incubated in oxygenated aCSF for ~1hr. The following PI3K pathway

429 inhibitors were dissolved in 100% DMSO and used *in vitro*: pan-PI3K inhibitor BKM120
430 (Buparlisib; Novartis, Switzerland; working concentration: ~3.5 μM); pan-AKT inhibitor
431 AZD5363 (Capivasertib; Selleckchem, USA; working concentration: 0.5 μM); MTOR
432 inhibitor RAD001 (Everolimus, Chem Express Cat# 159351-69-6; working
433 concentration: 0.52 μM).
434
435 **Western blotting**
436 Horizontal forebrain slices from 5 control and 5 mutant mice were obtained and
437 recovered in oxygenated aCSF as detailed above. Slices showing nice hippocampal
438 morphology were selected, treated for 1 hour with DMSO, BKM120, AZD5363 and
439 RAD001 respectively, in the same concentrations used for recording. The treated slices
440 were then flash-frozen in liquid nitrogen and stored at -80°C for post-processing. These
441 brain slices were lysed in NP-40 lysis buffer (150 mM NaCl, 50 mM Tris (pH 7.4), 1%
442 NP-40, 10 mM NaF, 2 mM sodium orthovanadate + protease/phosphatase inhibitor
443 cocktails [Sigma, USA]). Samples were normalized to equal protein concentrations
444 (0.333 mg/ml) using Pierce BCA protein assay (Thermo Fisher Scientific, USA).
445 Standards were made through serial dilutions of 10 mg/ml BSA. Samples were diluted
446 into a final concentration of 1x Laemmli sample buffer and boiled at 95°C for ten
447 minutes. 7.5% 10-well gels were prepared, and samples were run at 120V for 1.5 hours.
448 Gels were transferred onto polyvinylidene difluoride (Millipore) membranes and run
449 either overnight at 25V or for 2 hours at 60V. Membranes were blocked in 4% milk in
450 TBST (0.05 M Tris, 0.15 M NaCl, pH7.2, 0.1% (v/v) Tween20) for one hour at room
451 temperature, and primary antibodies were applied overnight at 4°C in blocking medium.

452 Primary antibodies for western blots were diluted as follows: rabbit anti-Phospho-AKT
453 Ser473 (D9E) (Cell Signaling Technology, USA; RRID: AB_2797780; 1:2000), mouse
454 anti-Pan-AKT (40D4) (Cell Signaling Technology, USA; Cat# 2920; 1:2000), rabbit anti-
455 Phospho-S6 Ribosomal Protein Ser235/236 (Cell Signaling Technology, USA; RRID:
456 AB_2721245, 1:2000), mouse anti-S6 Ribosomal Protein (54D2) (Cell Signaling
457 Technology, USA; RRID: AB_2238583, 1:1000), rabbit anti-beta(b)-Actin (GeneTex,
458 USA; RRID: AB_1949572, 1:10000). After washing and probing respectively with goat
459 anti-rabbit (RRID: AB_2313567) and anti-mouse (RRID: AB_10015289) horseradish
460 peroxidase (HRP)-conjugated secondary antibodies (1:10000; Jackson
461 ImmunoResearch Labs, USA), blots were imaged using Femto chemiluminescent
462 detection reagents (Thermo Fisher Scientific, USA; Cat# 34095) in a FluorChem R
463 western blot imaging system (ProteinSimple, Bio-Techne, USA). 8-bit images were used
464 as a representative western blot. 16-bit images were used to quantify the intensity of
465 each band using ImageJ v1.53. Regions of interest were drawn in each sample's lane.
466 After quantifying the lane in a histogram, the peak representing the band of interest was
467 isolated and the area of the region was measured as the band's quantification.
468

469 **Quantitative and Statistical Analyses**

470 Number of mice used was consistent with previous experiments completed and
471 published by us and other investigators. For extracellular field potential analyses,
472 baseline potential from integrated traces were measured for each [K^+] and normalized to
473 the value at 3 mM for each slice per genotype; relative peak amplitude was similarly
474 measured for control and mutant slices for 3,7,8,9 mM of [K^+]. In whole-cell patch-clamp

475 recording, plateau potential shift (PPS) was calculated by subtracting the baseline
476 potential from the highest plateau/burst potential in a paroxysmal depolarizing event.
477 Burst duration and inter-burst interval were measured as shown in Figure 3 – figure
478 supplement 1 and averaged across multiple bursts per cell. Input resistance was
479 measured from evoked current-clamp recordings by dividing the voltage difference
480 (measured at -10pA to -30pA I-steps) by the current interval (20pA). The decay
481 membrane time constant was obtained by recording the membrane response to 20pA
482 hyperpolarizing current pulses (300 ms duration, 1 Hz) and fitting the response to a
483 single exponential curve. We chose 20pA of hyperpolarizing current because such a
484 current intensity did not produce sag. Evoked spike frequencies and rheobase current
485 were calculated exclusively from tonic-firing cells. Burst threshold current was
486 calculated from burst-generating cells as the first current step which induced burst. *In*
487 *vitro* electrophysiological analyses were performed using Clampfit 10.7 and 11 (pClamp,
488 Molecular Devices, USA). For Western Blots, each band intensity was recalculated
489 relative to its respective b-actin band intensity, and then normalized across average
490 intensity per protein lane. Normalized ratios of phosphoproteins over total proteins were
491 thereafter obtained.
492 Statistical significance was assessed using 2-tailed unpaired t-tests with Welch's
493 correction (EEG power analyses, whole-cell RMP, burst duration, inter-burst interval,
494 Cd^{2+} data), 2-tailed paired t-tests (field potential baseline measurement, rheobase
495 current, drug-treated analyses) and ANOVA followed by Tukey post-tests (EEG
496 interictal spike frequency, field potential relative peak amplitude; whole-cell tonic spike
497 and burst frequencies, cell proportions, PPS, evoked spike frequency and time

498 constant; Western blots). Normal distribution was assumed for the data analyses, when
499 required. For EEG-ECoG-LFP experiments, quantitative and statistical data analysis
500 was performed in Labchart 8.2 software (AD Instruments, Colorado Spring, USA) and
501 Igor Pro 6.37 (WaveMetrics Inc., USA); final graphs were made in GraphPad Prism v7.0
502 (GraphPad Software Inc., San Diego, USA). For the remaining data, statistical analyses
503 and graph plotting were done using GraphPad Prism v7.0 and Microsoft Excel.
504 Differences were considered significant at $p<0.05$.
505
506
507 **Acknowledgments**

508 We thank Suzanne J. Baker for gifts of mouse lines (*Nestin-cre* and *Pik3ca*^{E545K}); Leon
509 Murphy (Novartis) for BKM120; Rory M. Murphy, Amanda P. Tran Hartman, Nikhil Sahai
510 and Jiyun Ryu for technical assistance; Aguan D. Wei and Paul Wakenight for
511 discussions. This work is funded by the NIH grants 1R01NS099027 (K.J.M.),
512 R01MH113545 (S.E.P.S.), R01NS102796 (F.K.), and CURE Sleep and Epilepsy Grant
513 (F.K.).
514
515 **Author Contributions:** A.R., F.K., J.M.R. and K.J.M. contributed to the study
516 conception and design. A.R., V.H., A.M.B., D.T.W. and F.K. contributed to the data
517 collection. A.R. and F.K. contributed to in vitro and in vivo data analyses respectively.
518 D.T.W. and S.E.P.S. contributed to Western blot data analyses and interpretation. A.R.,
519 F.K., J.M.R., K.J.M. contributed to the overall data interpretation. S.E.P.S., F.K. and
520 K.J.M. provided the funding resources. A.R. wrote the first draft of the manuscript and

521 others commented on previous versions of the manuscript. All authors read and
522 approved the final manuscript.
523
524 **Ethics**
525 Animal experimentation: All animal experimentation was conducted in accordance with
526 the guidelines laid down by the Institutional Animal Care and Use Committees (IACUC)
527 of Seattle Children's Research Institute, Seattle, WA, USA (protocol IDs: IACUC00006
528 (K.J.M.); IACUC00108 (F.K.)).

529 **REFERENCES**

530 Barker-Haliski, M., and H.S. White. 2019. 'Validated animal models for antiseizure drug (ASD) discovery:
531 Advantages and potential pitfalls in ASD screening', *Neuropharmacology*: 107750.
532 Bast, T., G. Ramantani, A. Seitz, and D. Rating. 2006. 'Focal cortical dysplasia: prevalence, clinical
533 presentation and epilepsy in children and adults', *Acta Neurol Scand*, 113: 72-81.
534 Berdichevsky, Y., A. M. Dryer, Y. Saponjian, M. M. Mahoney, C. A. Pimentel, C. A. Lucini, M. Usenovic,
535 and K. J. Staley. 2013. 'PI3K-Akt signaling activates mTOR-mediated epileptogenesis in
536 organotypic hippocampal culture model of post-traumatic epilepsy', *J Neurosci*, 33: 9056-67.
537 Blumcke, I., M. Thom, E. Aronica, D. D. Armstrong, H. V. Vinters, A. Palmini, T. S. Jacques, G. Avanzini, A.
538 J. Barkovich, G. Battaglia, A. Becker, C. Cepeda, F. Cendes, N. Colombo, P. Crino, J. H. Cross, O.
539 Delalande, F. Dubeau, J. Duncan, R. Guerrini, P. Kahane, G. Mathern, I. Najm, C. Ozkara, C.
540 Raybaud, A. Represa, S. N. Roper, N. Salamon, A. Schulze-Bonhage, L. Tassi, A. Vezzani, and R.
541 Spreafico. 2011. 'The clinicopathologic spectrum of focal cortical dysplasias: a consensus
542 classification proposed by an ad hoc Task Force of the ILAE Diagnostic Methods Commission',
543 *Epilepsia*, 52: 158-74.
544 Boissard, R., D. Gervasoni, M. H. Schmidt, B. Barbagli, P. Fort, and P. H. Luppi. 2002. 'The rat ponto-
545 medullary network responsible for paradoxical sleep onset and maintenance: a combined
546 microinjection and functional neuroanatomical study', *Eur J Neurosci*, 16: 1959-73.
547 Bolea, I., A. Gella, E. Sanz, P. Prada-Dacasa, F. Menardy, A. M. Bard, P. Machuca-Marquez, A. Eraso-
548 Pichot, G. Modol-Caballero, X. Navarro, F. Kalume, and A. Quintana. 2019. 'Defined neuronal
549 populations drive fatal phenotype in a mouse model of Leigh syndrome', *Elife*, 8.
550 Borck, C., and J. G. Jefferys. 1999. 'Seizure-like events in disinhibited ventral slices of adult rat
551 hippocampus', *J Neurophysiol*, 82: 2130-42.
552 Cardamone, M., D. Flanagan, D. Mowat, S. E. Kennedy, M. Chopra, and J. A. Lawson. 2014. 'Mammalian
553 target of rapamycin inhibitors for intractable epilepsy and subependymal giant cell astrocytomas
554 in tuberous sclerosis complex', *J Pediatr*, 164: 1195-200.
555 Chatzikonstantinou, A. 2014. 'Epilepsy and the hippocampus', *Front Neurol Neurosci*, 34: 121-42.
556 Cho, C. H. 2011. 'Frontier of epilepsy research - mTOR signaling pathway', *Exp Mol Med*, 43: 231-74.
557 Covey, E., J. A. Kauer, and J. H. Casseday. 1996. 'Whole-cell patch-clamp recording reveals subthreshold
558 sound-evoked postsynaptic currents in the inferior colliculus of awake bats', *J Neurosci*, 16:
559 3009-18.
560 Crino, P. B. 2016. 'The mTOR signalling cascade: paving new roads to cure neurological disease', *Nat Rev*
561 *Neurol*, 12: 379-92.
562 Curatolo, P., and R. Moavero. 2013. 'mTOR inhibitors as a new therapeutic option for epilepsy', *Expert*
563 *Rev Neurother*, 13: 627-38.
564 Davies, B. R., H. Greenwood, P. Dudley, C. Crafter, D. H. Yu, J. Zhang, J. Li, B. Gao, Q. Ji, J. Maynard, S. A.
565 Ricketts, D. Cross, S. Cosulich, C. C. Chresta, K. Page, J. Yates, C. Lane, R. Watson, R. Luke, D.
566 Ogilvie, and M. Pass. 2012. 'Preclinical pharmacology of AZD5363, an inhibitor of AKT:
567 pharmacodynamics, antitumor activity, and correlation of monotherapy activity with genetic
568 background', *Mol Cancer Ther*, 11: 873-87.
569 Dobyns, W. B., and G. M. Mirzaa. 2019. 'Megalencephaly syndromes associated with mutations of core
570 components of the PI3K-AKT-MTOR pathway: PIK3CA, PIK3R2, AKT3, and MTOR', *Am J Med*
571 *Genet C Semin Med Genet*, 181: 582-90.
572 Dudek, F. E., T. Yasumura, and J. E. Rash. 1998. ''Non-synaptic' mechanisms in seizures and
573 epileptogenesis', *Cell Biol Int*, 22: 793-805.
574 Filatov, G., G. P. Krishnan, N. F. Rulkov, and M. Bazhenov. 2011. 'Dynamics of epileptiform activity in
575 mouse hippocampal slices', *J Biol Phys*, 37: 347-60.

576 Forde, K., N. Resta, C. Ranieri, D. Rea, O. Kubassova, M. Hinton, K. A. Andrews, R. Semple, A. D. Irvine,
577 and V. Dvorakova. 2021. 'Clinical experience with the AKT1 inhibitor miransertib in two children
578 with PIK3CA-related overgrowth syndrome', *Orphanet J Rare Dis*, 16: 109.
579 Hughes, J. R. 2008. 'Gamma, fast, and ultrafast waves of the brain: their relationships with epilepsy and
580 behavior', *Epilepsy Behav*, 13: 25-31.
581 Kalume, F. 2013. 'Sudden unexpected death in Dravet syndrome: respiratory and other physiological
582 dysfunctions', *Respir Physiol Neurobiol*, 189: 324-8.
583 Kehne, J. H., B. D. Klein, S. Raeissi, and S. Sharma. 2017. 'The National Institute of Neurological Disorders
584 and Stroke (NINDS) Epilepsy Therapy Screening Program (ETSP)', *Neurochem Res*.
585 Kim, J. K., and J. H. Lee. 2019. 'Mechanistic Target of Rapamycin Pathway in Epileptic Disorders', *J Korean*
586 *Neurosurg Soc*, 62: 272-87.
587 Krueger, D. A., M. M. Care, K. Holland, K. Agricola, C. Tudor, P. Mangeshkar, K. A. Wilson, A. Byars, T.
588 Sahmoud, and D. N. Franz. 2010. 'Everolimus for subependymal giant-cell astrocytomas in
589 tuberous sclerosis', *N Engl J Med*, 363: 1801-11.
590 Kubista, H., S. Boehm, and M. Hotka. 2019. 'The Paroxysmal Depolarization Shift: Reconsidering Its Role
591 in Epilepsy, Epileptogenesis and Beyond', *Int J Mol Sci*, 20.
592 Lasarge, C. L., and S. C. Danzer. 2014. 'Mechanisms regulating neuronal excitability and seizure
593 development following mTOR pathway hyperactivation', *Front Mol Neurosci*, 7: 18.
594 Lee, S. A., D. D. Spencer, and S. S. Spencer. 2000. 'Intracranial EEG seizure-onset patterns in neocortical
595 epilepsy', *Epilepsia*, 41: 297-307.
596 Lehmann, J., J. Schneider, S. McPherson, D. E. Murphy, P. Bernard, C. Tsai, D. A. Bennett, G. Pastor, D. J.
597 Steel, C. Boehm, and et al. 1987. 'CPP, a selective N-methyl-D-aspartate (NMDA)-type receptor
598 antagonist: characterization in vitro and in vivo', *J Pharmacol Exp Ther*, 240: 737-46.
599 Leschinger, A., J. Stabel, P. Igelmund, and U. Heinemann. 1993. 'Pharmacological and electrographic
600 properties of epileptiform activity induced by elevated K+ and lowered Ca2+ and Mg2+
601 concentration in rat hippocampal slices', *Exp Brain Res*, 96: 230-40.
602 Lester, R. A., M. L. Quarum, J. D. Parker, E. Weber, and C. E. Jahr. 1989. 'Interaction of 6-cyano-7-
603 nitroquinoxaline-2,3-dione with the N-methyl-D-aspartate receptor-associated glycine binding
604 site', *Mol Pharmacol*, 35: 565-70.
605 Liautard, C., P. Scalmani, G. Carriero, M. de Curtis, S. Franceschetti, and M. Mantegazza. 2013.
606 'Hippocampal hyperexcitability and specific epileptiform activity in a mouse model of Dravet
607 syndrome', *Epilepsia*, 54: 1251-61.
608 Lindhurst, M. J., M. R. Yourick, Y. Yu, R. E. Savage, D. Ferrari, and L. G. Biesecker. 2015. 'Repression of
609 AKT signaling by ARQ 092 in cells and tissues from patients with Proteus syndrome', *Sci Rep*, 5:
610 17162.
611 Madsen, R. R. 2020. 'PI3K in stemness regulation: from development to cancer', *Biochem Soc Trans*, 48:
612 301-15.
613 Maira, S. M., S. Pecchi, A. Huang, M. Burger, M. Knapp, D. Sterker, C. Schnell, D. Guthy, T. Nagel, M.
614 Wiesmann, S. Brachmann, C. Fritsch, M. Dorsch, P. Chene, K. Shoemaker, A. De Pover, D.
615 Menezes, G. Martiny-Baron, D. Fabbro, C. J. Wilson, R. Schlegel, F. Hofmann, C. Garcia-
616 Echeverria, W. R. Sellers, and C. F. Voliva. 2012. 'Identification and characterization of NVP-
617 BKM120, an orally available pan-class I PI3-kinase inhibitor', *Mol Cancer Ther*, 11: 317-28.
618 Marcuccilli, C. J., A. K. Tryba, W. van Drongelen, H. Koch, J. C. Viemari, F. Pena-Ortega, E. L. Doren, P.
619 Pytel, M. Chevalier, A. Mrejeru, M. H. Kohrman, R. E. Lasky, S. M. Lew, D. M. Frim, and J. M.
620 Ramirez. 2010. 'Neuronal bursting properties in focal and parafocal regions in pediatric
621 neocortical epilepsy stratified by histology', *J Clin Neurophysiol*, 27: 387-97.
622 Mazumder, A. G., V. Patial, and D. Singh. 2019. 'Mycophenolate mofetil contributes to downregulation
623 of the hippocampal interleukin type 2 and 1beta mediated PI3K/AKT/mTOR pathway

624 hyperactivation and attenuates neurobehavioral comorbidities in a rat model of temporal lobe
625 epilepsy', *Brain Behav Immun*, 75: 84-93.
626 McCormick, D. A., and D. Contreras. 2001. 'On the cellular and network bases of epileptic seizures', *Annu*
627 *Rev Physiol*, 63: 815-46.
628 Meng, X. F., J. T. Yu, J. H. Song, S. Chi, and L. Tan. 2013. 'Role of the mTOR signaling pathway in epilepsy',
629 *J Neurol Sci*, 332: 4-15.
630 Mirzaa, G., Roy, A., Dobyns, W.B., Millen, K.J., Hevner, R.F. 2018. 'Hemimegalencephaly and Dysplastic
631 Megalencephaly' ' in Golden JA Adle-Biassette H, Harding BN (ed.), *Developmental*
632 *Neuropathology* (Wiley Blackwell).
633 Norris, D., P. Yang, S. Y. Shin, A. L. Kearney, H. J. Kim, T. Geddes, A. M. Senior, D. J. Fazakerley, L. K.
634 Nguyen, D. E. James, and J. G. Burchfield. 2021. 'Signaling Heterogeneity is Defined by Pathway
635 Architecture and Intercellular Variability in Protein Expression', *iScience*, 24: 102118.
636 Robinson, G., M. Parker, T. A. Kranenburg, C. Lu, X. Chen, L. Ding, T. N. Phoenix, E. Hedlund, L. Wei, X.
637 Zhu, N. Chalhoub, S. J. Baker, R. Huether, R. Kriwacki, N. Curley, R. Thiruvenkatam, J. Wang, G.
638 Wu, M. Rusch, X. Hong, J. Becksfort, P. Gupta, J. Ma, J. Easton, B. Vadodaria, A. Onar-Thomas, T.
639 Lin, S. Li, S. Pounds, S. Paugh, D. Zhao, D. Kawauchi, M. F. Roussel, D. Finkelstein, D. W. Ellison, C.
640 C. Lau, E. Bouffet, T. Hassall, S. Gururangan, R. Cohn, R. S. Fulton, L. L. Fulton, D. J. Dooling, K.
641 Ochoa, A. Gajjar, E. R. Mardis, R. K. Wilson, J. R. Downing, J. Zhang, and R. J. Gilbertson. 2012.
642 'Novel mutations target distinct subgroups of medulloblastoma', *Nature*, 488: 43-8.
643 Roy, A., K. J. Millen, and R. P. Kapur. 2020. 'Hippocampal granule cell dispersion: a non-specific finding in
644 pediatric patients with no history of seizures', *Acta Neuropathol Commun*, 8: 54.
645 Roy, A., R. M. Murphy, M. Deng, J. W. MacDonald, T. K. Bammler, K. A. Aldinger, I. A. Glass, and K. J.
646 Millen. 2019. 'PI3K-Yap activity drives cortical gyrification and hydrocephalus in mice', *Elife*, 8.
647 Roy, A., J. Skibo, F. Kalume, J. Ni, S. Rankin, Y. Lu, W. B. Dobyns, G. B. Mills, J. J. Zhao, S. J. Baker, and K. J.
648 Millen. 2015. 'Mouse models of human -related brain overgrowth have acutely treatable
649 epilepsy', *Elife*, 4:e12703.
650 Sanchez-Alegria, K., M. Flores-Leon, E. Avila-Munoz, N. Rodriguez-Corona, and C. Arias. 2018. 'PI3K
651 Signaling in Neurons: A Central Node for the Control of Multiple Functions', *Int J Mol Sci*, 19.
652 Shi, X., Y. Lim, A. K. Myers, B. L. Stallings, A. McCoy, J. Zeiger, J. Scheck, G. Cho, E. D. Marsh, G. M.
653 Mirzaa, T. Tao, and J. A. Golden. 2020. 'PIK3R2/Pik3r2 Activating Mutations Result in Brain
654 Overgrowth and EEG Changes', *Ann Neurol*, 88: 1077-94.
655 Stafstrom, C. E. 2019. *Developmental Epilepsy - From Clinical Medicine to Neurobiological Mechanisms*
656 (World Scientific).
657 Stafstrom, C. E., and L. Carmant. 2015. 'Seizures and epilepsy: an overview for neuroscientists', *Cold*
658 *Spring Harb Perspect Med*, 5.
659 Tryba, A. K., E. M. Merricks, S. Lee, T. Pham, S. Cho, D. R. Nordli, Jr., T. L. Eissa, R. R. Goodman, G. M.
660 McKhann, Jr., R. G. Emerson, C. A. Schevon, and W. van Drongelen. 2019. 'Role of paroxysmal
661 depolarization in focal seizure activity', *J Neurophysiol*, 122: 1861-73.
662 Venot, Q., T. Blanc, S. H. Rabia, L. Berteloot, S. Ladraa, J. P. Duong, E. Blanc, S. C. Johnson, C. Hoguin, O.
663 Boccara, S. Sarnacki, N. Boddaert, S. Pannier, F. Martinez, S. Magassa, J. Yamaguchi, B.
664 Knebelmann, P. Merville, N. Grenier, D. Joly, V. Cormier-Daire, C. Michot, C. Bole-Feysot, A.
665 Picard, V. Soupre, S. Lyonnet, J. Sadoine, L. Slimani, C. Chaussain, C. Laroche-Raynaud, L.
666 Guibaud, C. Broissand, J. Amiel, C. Legendre, F. Terzi, and G. Canaud. 2018. 'Targeted therapy in
667 patients with PIK3CA-related overgrowth syndrome', *Nature*, 558: 540-46.
668 Wang, Y., J. S. Greenwood, M. E. Calcagnotto, H. E. Kirsch, N. M. Barbaro, and S. C. Baraban. 2007.
669 'Neocortical hyperexcitability in a human case of tuberous sclerosis complex and mice lacking
670 neuronal expression of TSC1', *Ann Neurol*, 61: 139-52.

671 Wilcox, K. S., P. J. West, and C. S. Metcalf. 2020. 'The current approach of the Epilepsy Therapy
672 Screening Program contract site for identifying improved therapies for the treatment of
673 pharmacoresistant seizures in epilepsy', *Neuropharmacology*, 166: 107811.
674 Yang, J., J. Nie, X. Ma, Y. Wei, Y. Peng, and X. Wei. 2019. 'Targeting PI3K in cancer: mechanisms and
675 advances in clinical trials', *Mol Cancer*, 18: 26.
676 Yu, K., C. J. Lin, A. Hatcher, B. Lozzi, K. Kong, E. Huang-Hobbs, Y. T. Cheng, V. B. Beechar, W. Zhu, Y.
677 Zhang, F. Chen, G. B. Mills, C. A. Mohila, C. J. Creighton, J. L. Noebels, K. L. Scott, and B. Deneen.
678 2020. 'PIK3CA variants selectively initiate brain hyperactivity during gliomagenesis', *Nature*, 578:
679 166-71.
680 Zou, Z., T. Tao, H. Li, and X. Zhu. 2020. 'mTOR signaling pathway and mTOR inhibitors in cancer: progress
681 and challenges', *Cell Biosci*, 10: 31.

682

683 **TABLE**

684 **Table 1: Summary table of intrinsic membrane properties**

685 Summary of basic intrinsic membrane properties quantitated and compared between
686 control and mutant CA1 and CA3 neurons. No significant differences in RMP, input
687 resistance and rheobase current (minimum injected current required to elicit the first
688 action potential) were observed between control and mutant neurons, in both CA1 and
689 CA3. Decay time constant of mutant CA3 neurons was significantly longer than that of
690 control CA1 ($p < 0.0001$) and CA3 ($p = 0.0071$) cells, as well as of mutant CA1 neurons
691 ($p < 0.0001$) ($F=31.21$, $df=33$). Data is represented as mean ± SEM; differences were
692 considered significant at $p<0.05$.

693

#	Intrinsic properties	CA1		CA3	
		Control	Mutant	Control	Mutant
1	RMP (mV)	-55.36 ± 0.58	-54.64 ± 0.64	-56.07 ± 0.82	-56.49 ± 0.92
2	Input resistance (MΩ)	284.27 ± 21.6	262.82 ± 22.72	331.73 ± 23.54	272.99 ± 39.14
3	Time constant (ms)	21.79 ± 1.76	23.58 ± 1.85	32.23 ± 7.33	44.20 ± 4.56
4	Rheobase (pA)	11.54 ± 3.17	18.95 ± 3.66	18.95 ± 3.32	19.33 ± 4.19

694 **FIGURE LEGENDS**

695 **Figure 1: *Nestin-cre;Pik3ca^{E545K}* mutant brains show higher neural excitability**

696 (**A**) Schematic shows electrode placement for EEG-ECoG recordings in ~P70 *Nestin-*
697 *cre;Pik3ca^{E545K}* and control littermates. LFP, local field potential. (**B,C**) Compared to
698 controls, the mutants showed significantly higher frequency of regional (r) spikes and
699 train of spikes/polyspikes in neocortex (black traces) and hippocampus (blue traces).
700 (**D**) In the mutant, interictal spike frequency was significantly higher in hippocampus
701 (blue box), compared to those generated in neocortex (orange box) or generalized in
702 both regions (green box) (F=46.65, degrees of freedom (df)=27). (**E,F**) Power spectrum
703 analysis displayed increased activity in mutant, as emphasized in the representative
704 magnified segments. (**G,H**) Mutant hippocampus demonstrated significant higher
705 activity in the gamma frequency range (F=3.932, df=27; neocortex: F=26.93, df=27).
706 Data is represented as mean ± SEM scatter plots; differences were considered
707 significant at $p<0.05$; ns, not significant. Scalebars: 0.2s,20μV (B,C); 1s,50μV (E,F). See
708 also Figure 1 – figure supplement 1.

709

710 **Figure 2: Extracellular mutant CA1 recordings demonstrate hyper-**
711 **synchronization**

712 (**A**) Schematized flowchart summarizes the acute coronal brain slicing for extracellular
713 field potential recording. (**B,C**) Representative control (black) and mutant (red) voltage
714 and integrated voltage traces across a [K^+] gradient; comparison indicated significantly
715 higher excitability in the mutant brain. (**D,E**) Acute extracellular BKM120 administration
716 at constant 7mM [K^+] aCSF suppressed synchronized ictal bursts in mutant CA1 field

717 within ~20-30min, with minimal effect on the control hippocampal slices. Scalebars:
718 2min,0.5V (B-E). See also Figure 2 – figure supplement 1.
719
720 **Figure 3: Mutant hippocampal neurons produce increased epileptiform burst**
721 **activity**
722 (**A**) Flowchart shows acute horizontal brain slicing for whole-cell recording. (**B-E**) Traces
723 represent silent, tonic, and burst categories of CA1 and CA3 neurons based on
724 spontaneous cellular activity; respective pie charts marked proportion of recorded cells.
725 Mutant CA1 and CA3 exhibited significantly higher proportions of burst-firing cells
726 compared to controls. Significantly fewer tonic-firing cells were observed in mutant CA1.
727 (**F,G**) relative to controls, spontaneous tonic spike frequencies were significantly higher
728 in mutant CA1 (t=2.175, df=43.71) and CA3 (t=4.063, df=19.78) cells; burst frequency
729 was significantly higher in mutant CA1 (CA1: t=2.244, df=29.38; CA3: t=0.1561,
730 df=6.754). (**H**) Plateau potential shift (PPS) in mutant bursting cells, as depicted in (**H'**),
731 was significantly higher in CA1 (t=2.586, df=8.118) but similar in CA3 (t=0.2436,
732 df=5.110), compared to respective controls. (**I-L**) Representative evoked voltage traces
733 of control and mutant showed tonic and burst firing in response to current steps. (**M**)
734 Evoked recording also marked significantly higher bursting cell proportions in the
735 mutant. Data is represented as pie charts, % bar graphs and mean ± SEM scatter plots;
736 differences were considered significant at $p<0.05$; ns, not significant. Scalebars:
737 1s,20mV (B,D); 0.1s,20mV (H', I-L). See also Figure 3 – figure supplements 1-2.
738

739 **Figure 4: Pik3ca-related burst characteristics are dependent on cell-intrinsic**
740 **calcium and potassium channel regulation**
741 (**A-D**) Blocking calcium channels by extracellular cadmium (Cd^{2+}) significantly altered
742 intrinsic bursting pattern of mutant neurons including burst frequency (t=3.267, df=3)
743 and PPS (t=4.172, df=3). (**E-H**) Representative traces and respective pie charts show
744 types of cellular activity in control and mutant CA1 and CA3 neurons after administering
745 cesium intracellularly. In response to cesium, tonic firing cells were significantly reduced
746 and original differences in CA1 and CA3 cell proportions between control and mutant
747 were normalized. (**I**) Cs^{+}-induced burst frequency was significantly higher in mutant CA3
748 than those in respective controls (F= 26.31, df=21); unlike normal spontaneous state, no
749 such difference was observed in CA1. (**J-L**) Intracellular cesium lowered the
750 spontaneously enhanced mutant PPS in CA1 to control levels (F=4.003, df=20), while
751 having no effect on RMP (CA1: t=1.308, df=27.32; CA3: t=0.2616, df=6.816) or input
752 resistance (F= 2.936, df=42) in both control and mutant neurons. Data is represented as
753 pie charts, % bar graphs and mean ± SEM scatter plots; differences were considered
754 significant at $p<0.05$; ns, not significant. Scalebars: 1s,20mV (A,E,F). See also Figure 4
755 – figure supplement 1.
756
757 **Figure 5: Acute inhibition of Pik3ca or Akt suppresses hyperactivity in mutant**
758 **cells**
759 (**A**) Schematic of simplified PI3K-AKT-MTOR pathway, marking targets of action for
760 BKM120, AZD5363 and RAD001. Representative traces demonstrate differential action
761 of BKM120 (**B**), AZD5363 (**F**) and RAD001 (**J**) on *Nestin-cre;Pik3ca*^{E545K} hippocampal

762 neurons, ranging from being unaffected to change in frequency/pattern to silencing, as
763 quantitated respectively in (**C,G,K**). (**D,E,H,I**) BKM120 and AZD5363 significantly
764 reduced mutant burst frequency (BKM120: F=8.937, df=38; AZD5363: F=43.50, df=20)
765 and PPS (BKM120: F=24.39, df=36; AZD5363: t=6.386, df=6) in both CA1 and CA3.
766 (**E',I'**) Insets show activity traces of mutant bursting cell before (red) and after BKM120
767 (blue) or AZD5363 (pink) administration. (**L,M**) Acute RAD001 treatment had no overt
768 effect on the mutant burst frequency (t=0.4414, df=4) or PPS (t=0.7692, df=4). Data is
769 represented as % bar graphs and mean ± SEM scatter plots; differences were
770 considered significant at $p<0.05$; ns, not significant. Scalebars: 1s,20mV (B,F,J);
771 0.05s,20mV (E',I'). See also Figure 5 – figure supplements 1-2.
772

773 **Figure Supplements**

774 **Figure 1 – figure supplement 1: ECoG-LFP traces show different types of**
775 **epileptiform activity in *Nestin-cre;Pik3ca*^{E545K} brains**

776 (**A,B**) Examples of different types of isolated spiking events in the neocortex and
777 hippocampus taken from 2 different mutant mice showed a varied range of spike nature
778 – in frequency, source of origin and amplitude. (**C**) Example of train of spiking events in
779 the hippocampus and left cortex. (**D**) Example of low amplitude, high frequency
780 brushing events. g, generalized; r, regional. Scalebars: 0.5s,50mV (A,B); 2s,50mV
781 (C,D).

782

783 **Figure 2 – figure supplement 1: Enhanced neuronal network excitability in mutant**
784 **CA1 across an extracellular potassium gradient**

785 (**A**) Bar graphs depicted normalized baseline shift of integrated field potential traces in
786 the mutant with increasing [K^+] (refer to Figure 2). The mutant baseline was significantly
787 higher than that of control especially in the 9-11mM range (t=3.343, degrees of freedom
788 (df)=9). (**B**) Relative peak amplitude of mutant spiking was significantly higher than
789 controls at higher potassium concentrations (F=266.1; df=564). Data is represented as
790 mean ± SEM bar graphs; differences were considered significant at $p<0.05$; ns, not
791 significant.

792

793 **Figure 3 – figure supplement 1: Spontaneous burst-firing features of control and**
794 **mutant pyramidal neurons**

795 (**A**) Representative traces for subtypes of burst firing, namely burst cluster, paroxysmal
796 depolarization shift (PDS) and non-PDS plateau bursts. (**B**) Proportion of burst

797 subcategories were not overtly different in control and mutant CA1 and CA3 regions (F=
798 $7.355e^{-12}$; df=6); burst clusters were only seen in mutant cells. (**C**) Representative trace
799 demonstrates how burst duration and inter-burst interval were calculated. (**D,E**) In both
800 CA1 and CA3, average (avg.) burst duration (CA1: t=0.9644, df=6.793; CA3: t=0.3508,
801 df=6.229) and inter-burst interval (CA1: t=0.1263, df=22.31; CA3: t=1.485, df=10.73)
802 were not significantly different between control and mutant neurons. Data is represented
803 as mean ± SEM scatter plots; differences were considered significant at $p<0.05$; ns, not
804 significant; PPS, plateau potential shift. Scalebars: 0.2s,20mV (a), 1s,20mV (c).
805
806 **Figure 3 – figure supplement 2: Resting membrane potentials and threshold**
807 **currents for hippocampal neuronal firing remain unchanged by Pik3ca**
808 **overactivation**
809 (**A-C**) Resting membrane potential (RMP) was not significantly different between control
810 and mutant neurons, both in CA1 (t=0.8331, df=94.99) and CA3 (t=0.3438, df=78.53),
811 as well as among different firing types (CA1: F=0.9136, df=90; CA3: F=2.829, df=75).
812 (**D,E**) No significant differences in evoked tonic spike frequencies were observed in the
813 tested range of input depolarizing current (0-90pA), between control and mutant CA1
814 and CA3 neurons (CA1: F=13.07, df=320; CA3: F=4.844, df=270). (**F**) No overt
815 differences in the current inducing the first burst were observed between control and
816 mutant (CA1: t=1.744, df=20.29; CA3: t=0.8493, df=2.439). Data is represented as
817 mean ± SEM scatter and line plots; differences were considered significant at $p<0.05$;
818 ns, not significant.
819

820 **Figure 4 – figure supplement 1: Pik3ca-related epileptiform activity is not**
821 **dependent on glutamatergic or GABAergic inputs**
822 (**A**) Representative spontaneous mutant trace and traces of the same cell post-
823 treatment with glutamatergic receptor antagonists (CPP, CNQX) and with GABA
824 antagonist gabazine showed no significant change in firing pattern. (**B-D**) Large
825 proportion of mutant cells remained unaffected after being blocked from external
826 glutamatergic or GABAergic inputs. (**E-L**) No significant differences in normalized
827 plateau potential shift (PPS; CPP: F=3.391, df=12; CNQX: F=1.432, df=12; Gabazine:
828 t=0.3904, df=4) or in tonic (CPP: t=1.876, df=7; CNQX: F=0.2766, df=20; Gabazine:
829 F=0.0001130, df=16) and burst frequencies (CPP: F=0.5140, df=16; CNQX: F=5.218,
830 df=16) were observed before and after administration of channel blockers. Data is
831 represented as % bar graphs and mean ± SEM scatter plots; differences were
832 considered significant at $p<0.05$; ns, not significant. Scalebar: 1s,20mV (A).
833
834 **Figure 5 – figure supplement 1: Acute treatment with BKM120 and AZD5363 has**
835 **differential effect on *Nestin-cre;Pik3ca^{E545K}* neuronal physiological properties**
836 (**A-D**) Acute BKM120 treatment did not significantly affect RMP (F=0.9268, df=42), tonic
837 rheobase current (t=0.000, df=8), average burst duration (CA1: t=1.264, df=8; CA3:
838 t=0.6150, df=11) or inter-burst interval (CA1: t=1.889, df=8; CA3: t=1.160, df=10) in
839 mutant hippocampal neurons. (**E-H**) Acute AKT inhibition by AZD5363 had no effect on
840 the mutant RMP (F=0.3316, df=20) or rheobase current (t=0.3859, df=7), but
841 significantly attenuated the average burst duration (t=4.052, df=5) and inter-burst
842 interval (t=4.597, df=6), largely by suppressing bursts or silencing the cells. (**I,J**) Plots

843 marked percentage of mutant CA3 “bursting” cells undergoing changes as a function of
844 time, in response to acute administration of BKM120 (I) and AZD5363 (J). (**K**) Mutant
845 plateau frequency significantly dropped as a function of time, where 0min marked the
846 time of administration of BKM120/AZD5363 onto the brain slice. Data is represented as
847 mean ± SEM scatter plots; differences were considered significant at $p<0.05$; ns, not
848 significant.
849
850 **Figure 5 – figure supplement 2: Acute treatment with RAD001 has no overt effect**
851 **on mutant neuronal physiological properties**
852 (**A-D**) Acute BKM120 treatment did not significantly affect the RMP (t=1.327, df=4),
853 average burst duration (t=1.073, df=4), inter-burst interval (t=0.4023, df=4) or rheobase
854 current (t=1.000, df=4) in mutant CA1 neurons. (**E**) Representative Western blots bands
855 of pAKT_S473, pan-AKT, pS6-S235/236 and RPS6 (total S6) are demonstrated across
856 different treatment (DMSO, BKM120, AZD5363, RAD001). (**F,G**) Quantifications of
857 normalized ratios of phosphoproteins over total proteins showed significant reduction of
858 pAKT_S473 in response to acute BKM120 and RAD001 treatment but not post-
859 AZD5363 (F=22.98, df=32); pS6_S235/236 in mutant had a decreasing trend in
860 response to all pathway drugs (F=4.485, df=32). Data is represented as mean ± SEM
861 scatter plots and bar graphs; differences were considered significant at $p<0.05$; ns, not
862 significant.

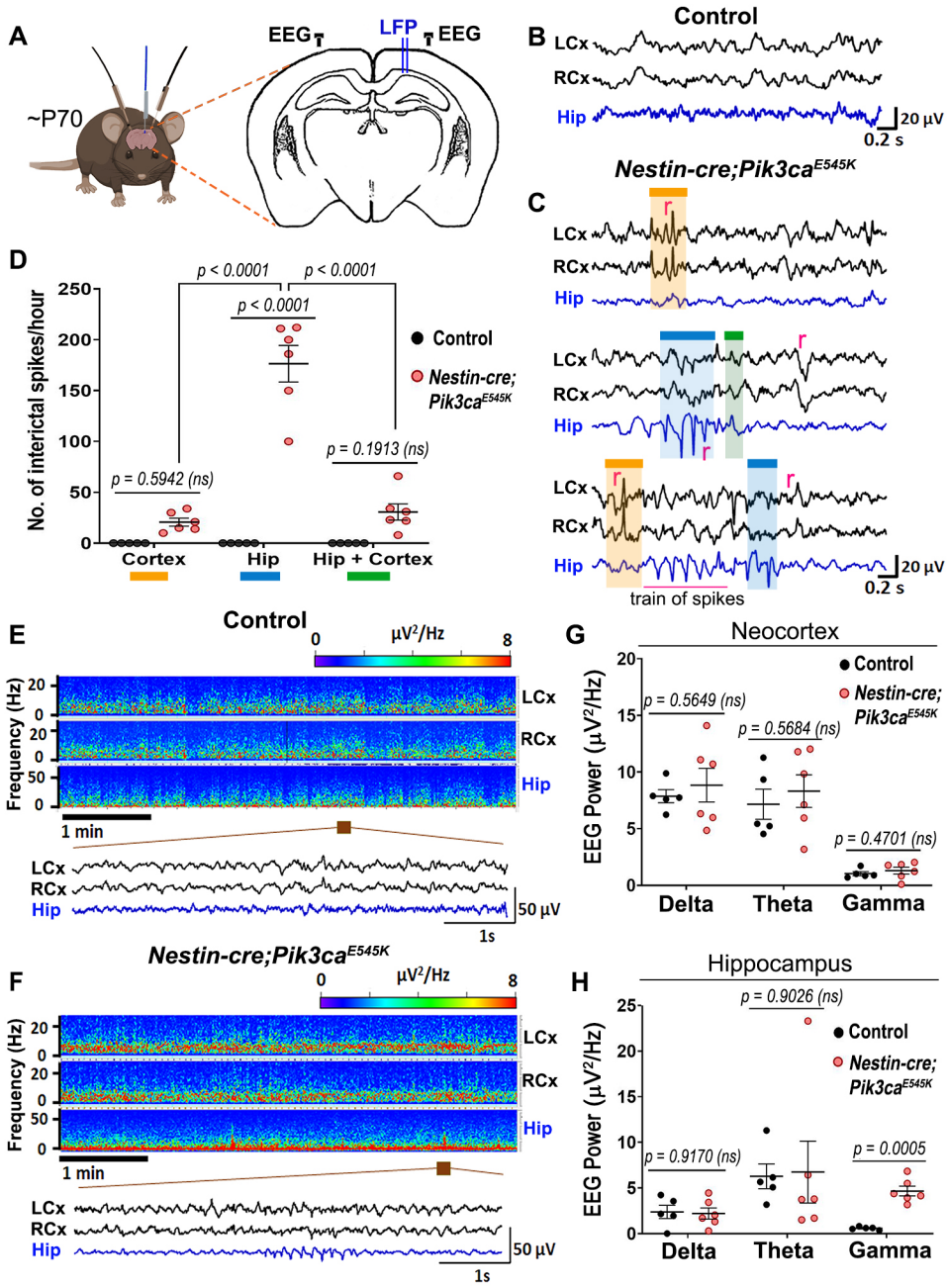
A
~P70
EEG
LFP
EEG
B
Control
LCx
RCx
Hip
20 µV
0.2 s
C
Nestin-cre;Pik3ca^E545K
LCx
RCx
Hip
train of spikes
20 µV
0.2 s
D
No. of interictal spikes/hour
p < 0.0001
p < 0.0001
p < 0.0001
p = 0.5942 (ns)
p = 0.1913 (ns)
Control
Nestin-cre; Pik3ca^E545K
Cortex
Hip
Hip + Cortex
E
Control
µV²/Hz
0
8
Frequency (Hz)
LCx
RCx
Hip
1 min
50 µV
1s
F
Nestin-cre;Pik3ca^E545K
µV²/Hz
0
8
Frequency (Hz)
LCx
RCx
Hip
1 min
50 µV
1s
G
Neocortex
EEG Power (µV²/Hz)
p = 0.5649 (ns)
p = 0.5684 (ns)
p = 0.4701 (ns)
Control
Nestin-cre; Pik3ca^E545K
Delta
Theta
Gamma
H
Hippocampus
EEG Power (µV²/Hz)
p = 0.9026 (ns)
p = 0.9170 (ns)
p = 0.0005
Control
Nestin-cre; Pik3ca^E545K
Delta
Theta
Gamma

Figure 1

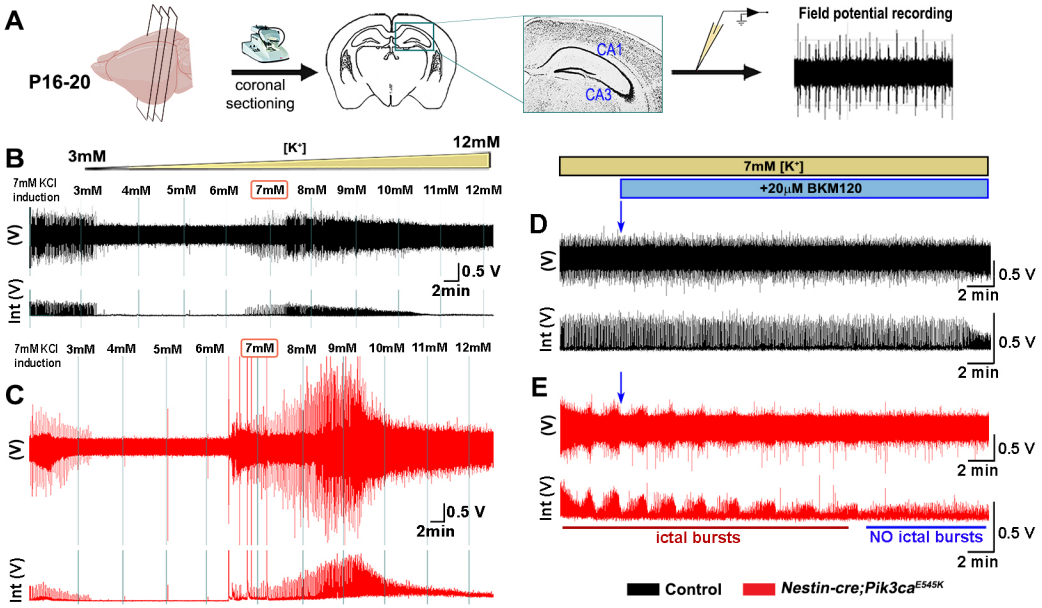
A
P16-20
coronal
sectioning
CA1
CA3
Field potential recording
B
3mM
[K+]
12mM
7mM KCl
induction
3mM 4mM 5mM 6mM 7mM 8mM 9mM 10mM 11mM 12mM
(V)
0.5 V
2min
Int (V)
C
D
7mM [K+]
+20μM BKM120
2 min
E
ictal bursts
NO ictal bursts
Control
Nestin-cre;Pik3ca^{E545K}

Figure 2

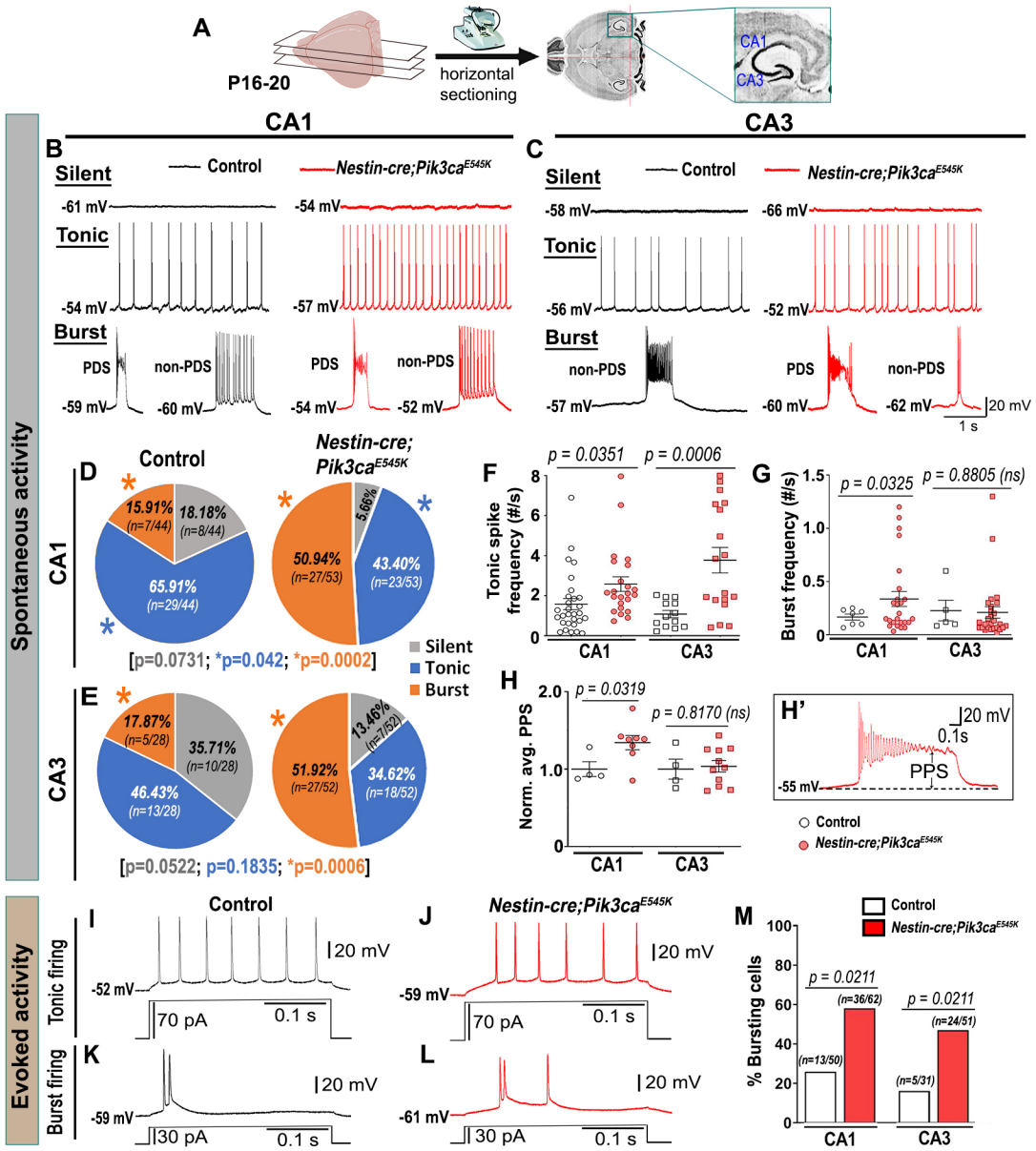
A
P16-20
horizontal sectioning
CA1
CA3
Spontaneous activity
B
CA1
Silent
Control
Nestin-cre;Pik3ca^E545K
-61 mV
-54 mV
Tonic
-54 mV
-57 mV
Burst
PDS
non-PDS
-59 mV
-60 mV
-54 mV
-52 mV
C
CA3
Silent
-58 mV
-66 mV
Tonic
-56 mV
-52 mV
Burst
non-PDS
-57 mV
PDS
non-PDS
-60 mV
-62 mV
20 mV
1 s
D
Control
Nestin-cre; Pik3ca^E545K
CA1
15.91% (n=7/44)
18.18% (n=8/44)
65.91% (n=29/44)
5.66%
50.94% (n=27/53)
43.40% (n=23/53)
[p=0.0731; *p=0.042; *p=0.0002]
Silent
Tonic
Burst
E
CA3
17.87% (n=5/28)
35.71% (n=10/28)
46.43% (n=13/28)
13.46% (n=7/52)
51.92% (n=27/52)
34.62% (n=18/52)
[p=0.0522; p=0.1835; *p=0.0006]
F
p = 0.0351
p = 0.0006
Tonic spike frequency (#/s)
CA1
CA3
G
p = 0.0325
p = 0.8805 (ns)
Burst frequency (#/s)
CA1
CA3
H
p = 0.0319
p = 0.8170 (ns)
Norm. avg. PPS
CA1
CA3
H'
20 mV
0.1s
PPS
-55 mV
Control
Nestin-cre;Pik3ca^E545K
Evoked activity
Tonic firing
I
Control
-52 mV
20 mV
70 pA
0.1 s
J
Nestin-cre;Pik3ca^E545K
-59 mV
20 mV
70 pA
0.1 s
Burst firing
K
-59 mV
20 mV
30 pA
0.1 s
L
-61 mV
20 mV
30 pA
0.1 s
M
Control
Nestin-cre;Pik3ca^E545K
% Bursting cells
p = 0.0211
(n=36/62)
(n=13/50)
p = 0.0211
(n=24/51)
(n=5/31)
CA1
CA3

Figure 3

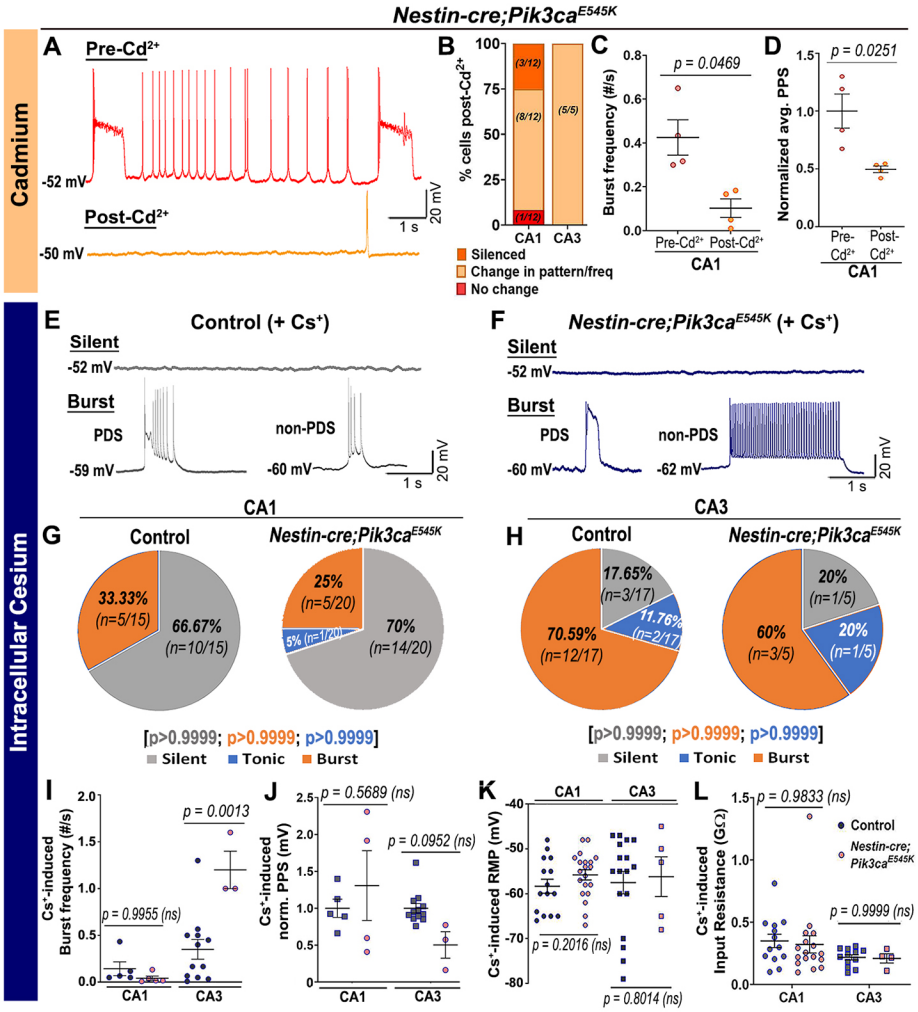
Nestin-cre;Pik3ca^{E545K}
Cadmium
A
Pre-Cd^{2+}
-52 mV
Post-Cd^{2+}
-50 mV
1 s
20 mV
B
% cells post-Cd^{2+}
(3/12)
(8/12)
(1/12)
(5/5)
CA1
CA3
Silenced
Change in pattern/freq
No change
C
p = 0.0469
Burst frequency (#/s)
Pre-Cd^{2+}
Post-Cd^{2+}
CA1
D
p = 0.0251
Normalized avg. PPS
Pre-Cd^{2+}
Post-Cd^{2+}
CA1
Intracellular Cesium
E
Control (+ Cs^{+})
Silent
-52 mV
Burst
PDS
-59 mV
non-PDS
-60 mV
1 s
20 mV
F
Nestin-cre;Pik3ca^{E545K} (+ Cs^{+})
Silent
-52 mV
Burst
PDS
-60 mV
non-PDS
-62 mV
1 s
20 mV
CA1
G
Control
Nestin-cre;Pik3ca^{E545K}
33.33% (n=5/15)
66.67% (n=10/15)
25% (n=5/20)
5% (n=1/20)
70% (n=14/20)
[p>0.9999; p>0.9999; p>0.9999]
Silent
Tonic
Burst
CA3
H
Control
Nestin-cre;Pik3ca^{E545K}
17.65% (n=3/17)
11.76% (n=2/17)
70.59% (n=12/17)
20% (n=1/5)
60% (n=3/5)
20% (n=1/5)
[p>0.9999; p>0.9999; p>0.9999]
Silent
Tonic
Burst
I
Cs^{+}-induced Burst frequency (#/s)
p = 0.0013
p = 0.9955 (ns)
CA1
CA3
J
Cs^{+}-induced norm. PPS (mV)
p = 0.5689 (ns)
p = 0.0952 (ns)
CA1
CA3
K
Cs^{+}-induced RMP (mV)
CA1
CA3
p = 0.2016 (ns)
p = 0.8014 (ns)
L
Cs^{+}-induced Input Resistance (GΩ)
p = 0.9833 (ns)
p = 0.9999 (ns)
Control
Nestin-cre; Pik3ca^{E545K}
CA1
CA3

Figure 4

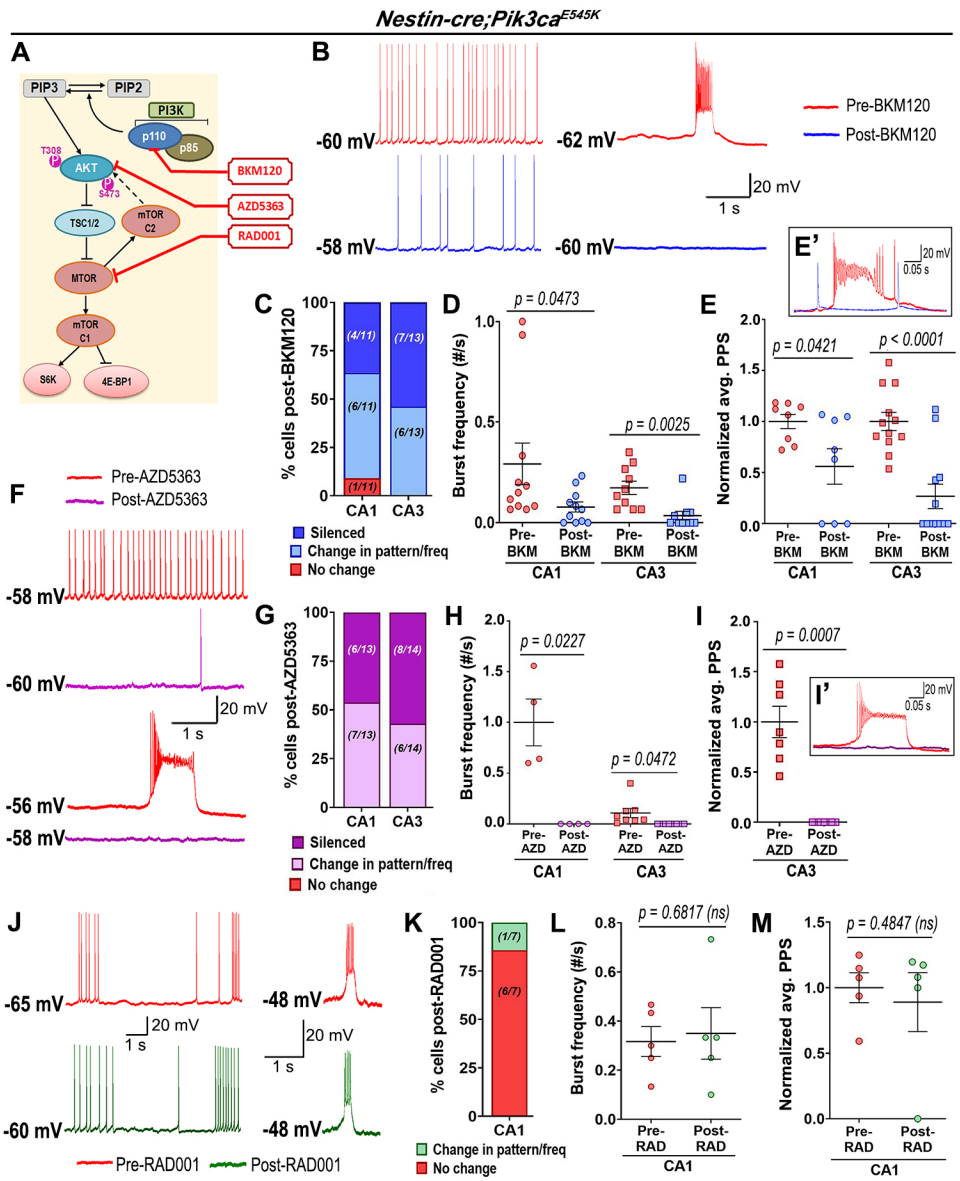
Nestin-cre;Pik3ca^{E545K}
A
PIP3
PIP2
PI3K
p110
p85
T308
AKT
S473
TSC1/2
mTOR C2
MTOR
mTOR C1
S6K
4E-BP1
BKM120
AZD5363
RAD001
B
-60 mV
-58 mV
-62 mV
-60 mV
Pre-BKM120
Post-BKM120
20 mV
1 s
E'
20 mV
0.05 s
C
% cells post-BKM120
(4/11)
(6/11)
(1/11)
(7/13)
(6/13)
CA1
CA3
Silenced
Change in pattern/freq
No change
D
Burst frequency (#/s)
p = 0.0473
p = 0.0025
Pre-BKM
Post-BKM
CA1
CA3
E
Normalized avg. PPS
p = 0.0421
p < 0.0001
Pre-BKM
Post-BKM
CA1
CA3
F
Pre-AZD5363
Post-AZD5363
-58 mV
-60 mV
20 mV
1 s
-56 mV
-58 mV
G
% cells post-AZD5363
(6/13)
(7/13)
(8/14)
(6/14)
CA1
CA3
Silenced
Change in pattern/freq
No change
H
Burst frequency (#/s)
p = 0.0227
p = 0.0472
Pre-AZD
Post-AZD
CA1
CA3
I
Normalized avg. PPS
p = 0.0007
I'
20 mV
0.05 s
Pre-AZD
Post-AZD
CA3
J
-65 mV
-48 mV
20 mV
1 s
20 mV
1 s
-60 mV
-48 mV
Pre-RAD001
Post-RAD001
K
% cells post-RAD001
(1/7)
(6/7)
CA1
Change in pattern/freq
No change
L
Burst frequency (#/s)
p = 0.6817 (ns)
Pre-RAD
Post-RAD
CA1
M
Normalized avg. PPS
p = 0.4847 (ns)
Pre-RAD
Post-RAD
CA1

Figure 5

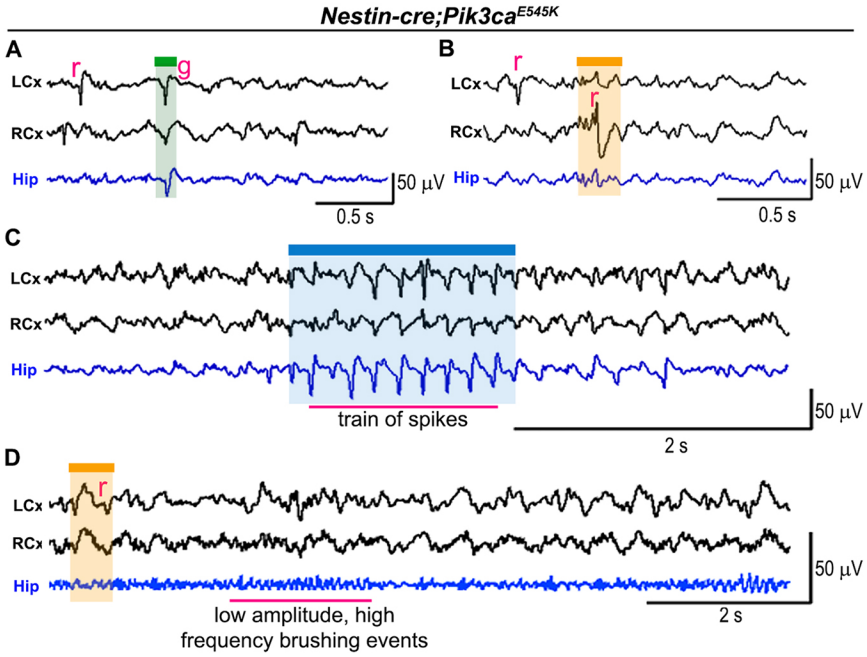

Figure 1 - figure supplement 1

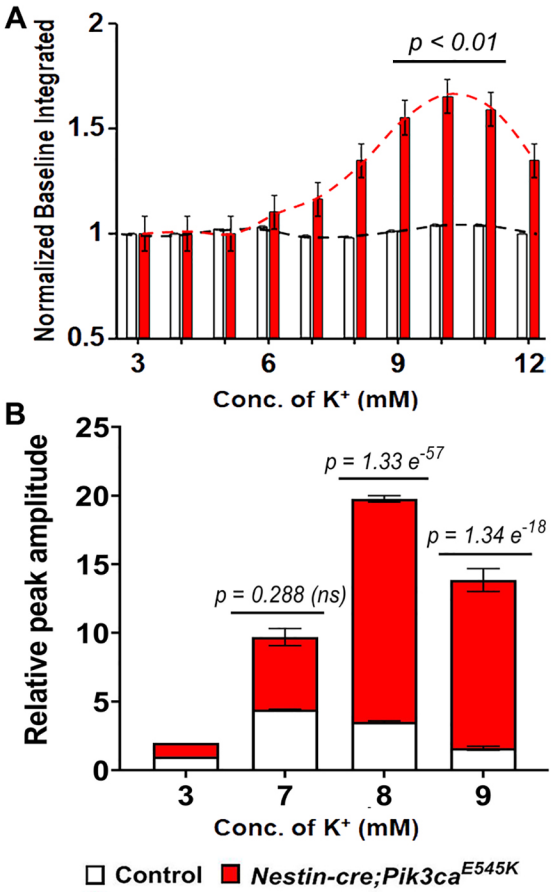

Figure 2 - figure supplement 1

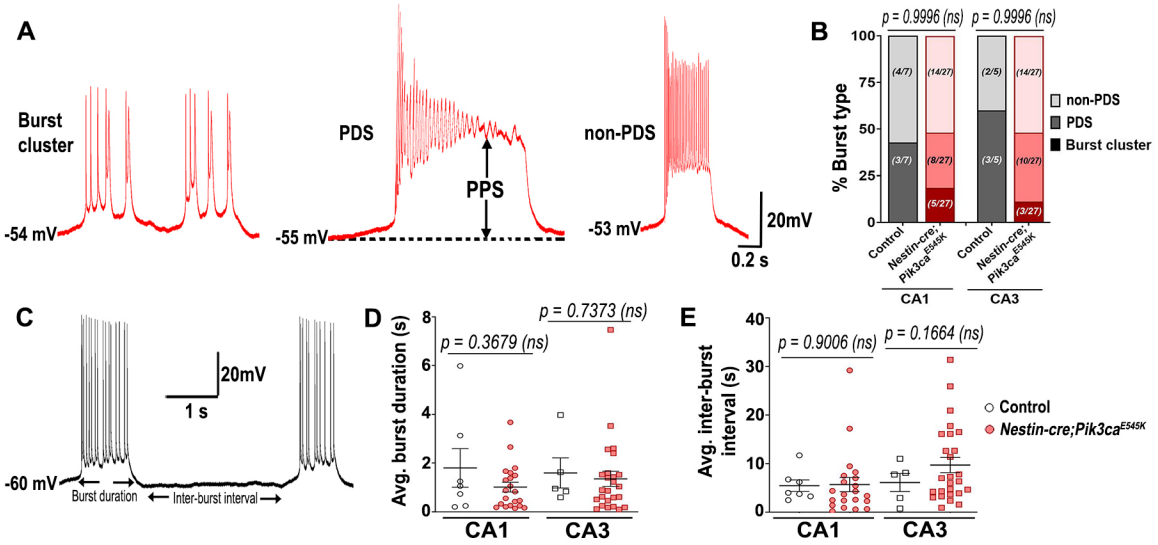

Figure 3 – figure supplement 1

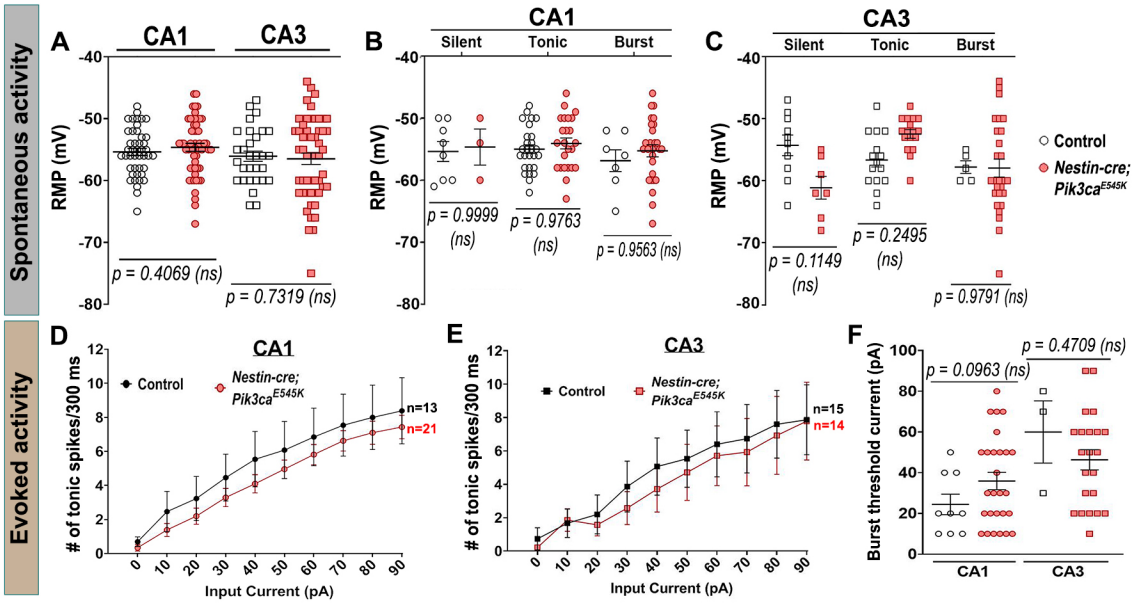

Figure 3 - figure supplement 2

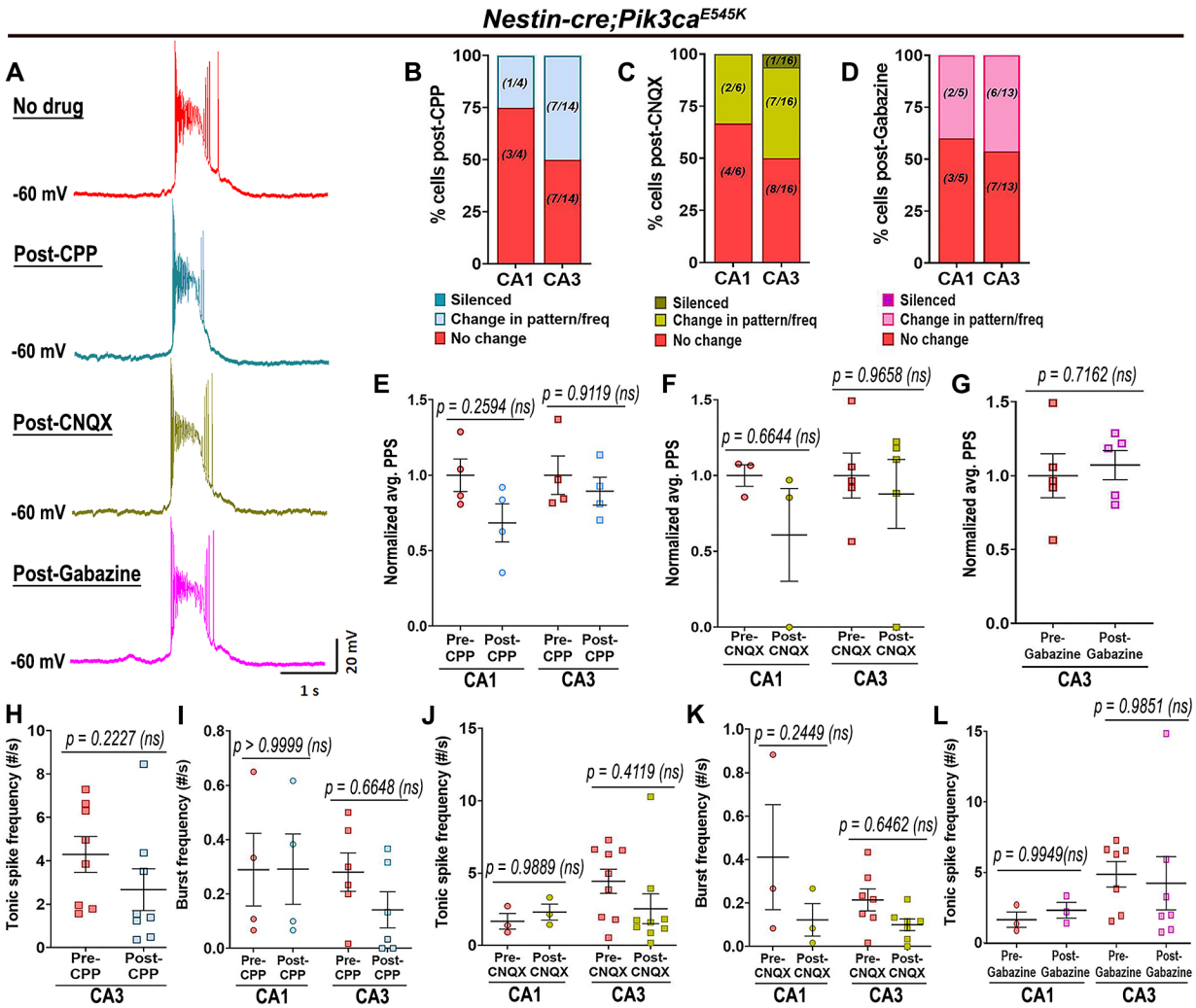

Figure 4 - figure supplement 1

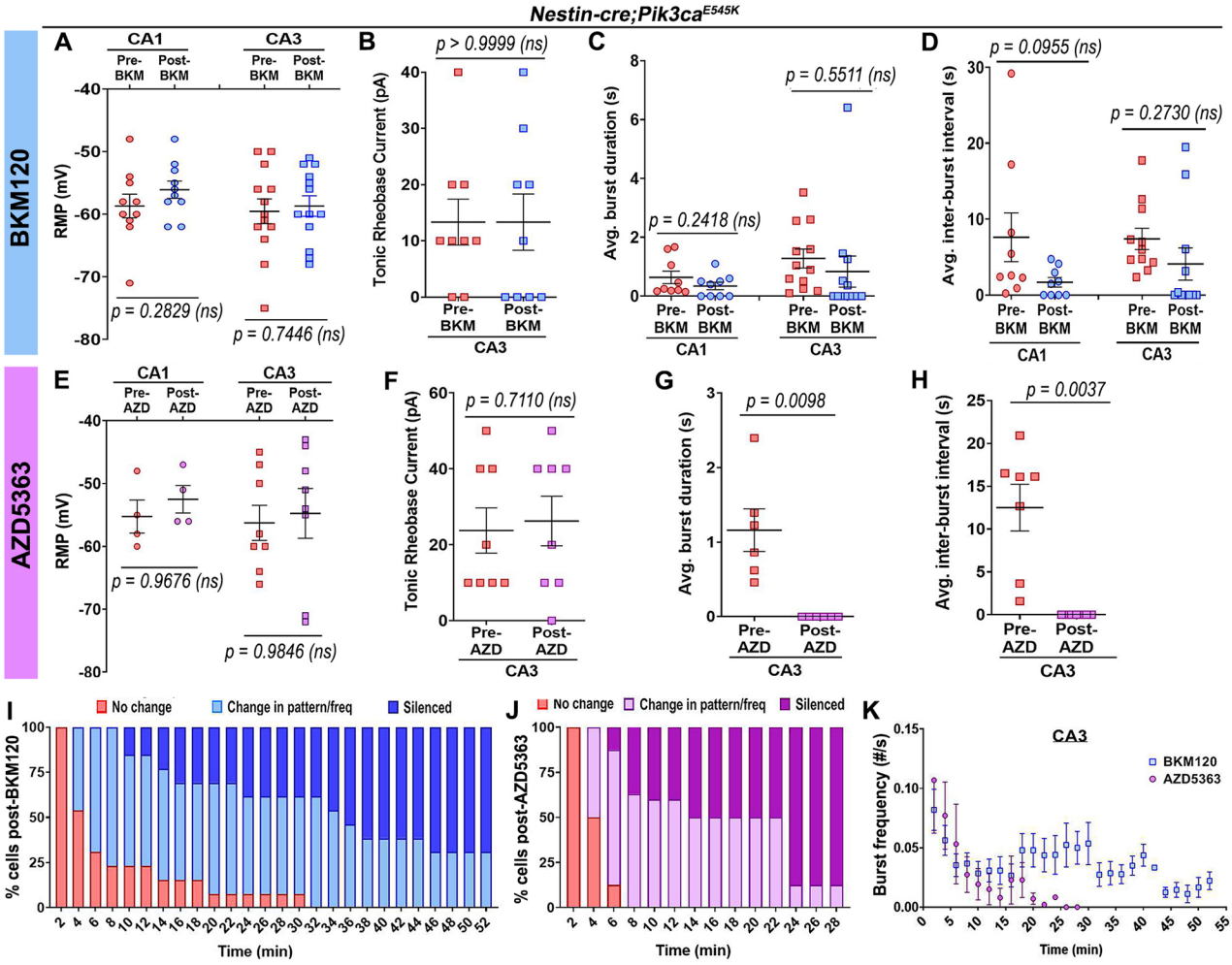

Figure 5 - figure supplement 1

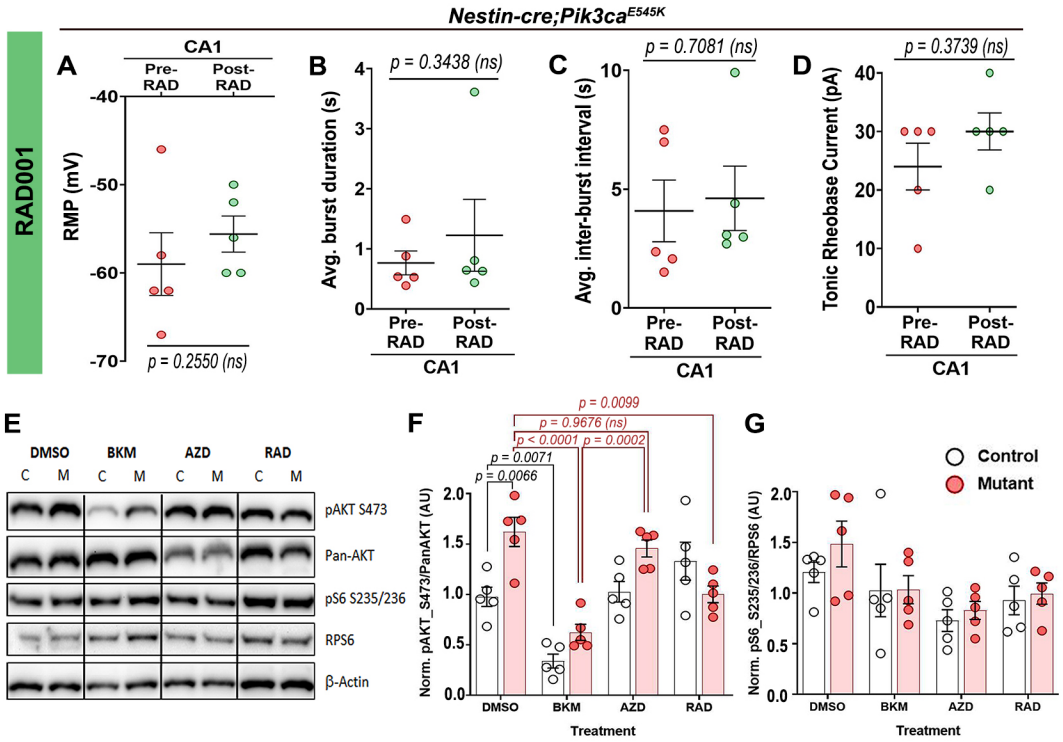

Figure 5 - figure supplement 2